Seismic Hazard Assessment for the Korean Peninsula

Seongjun Park[1], Tae-Kyung Hong*[1], and Gyubyeong Rah[1]

ABSTRACT

The Korean Peninsula is located in a stable intraplate region with low-seismicity rates and long recurrence intervals of major earthquakes. Recent moderate-size earthquakes demonstrate possible occurrence of seismic damages in the Korean Peninsula. A probabilistic seismic hazard analysis based on instrumental and historical seismicity is applied for the Korean Peninsula. Three seismotectonic province models are used for area sources. Seven ground-motion prediction equations calibrated for bedrock condition are considered. Fault source models are not applied due to poor identification of active faults. A 500 yr long historical record of earthquakes includes moderate and large earthquakes of long recurrence intervals. The influences of model parameters are reflected through a logic-tree scheme. The process and results are verified by Monte Carlo ground-motion level simulation and benchmark tests. Relatively high-seismic hazards are modeled in the northwestern, south-central, and southeastern Korean Peninsula. The horizontal peak ground accelerations reach ~0.06, 0.09, 0.13, 0.21, and 0.28*g* for periods of 25, 50, 100, 250, and 500 yr, respectively, with exceedance probability of 10%. Successive moderate-size earthquakes since the 11 March 2011 Tohoku–Oki megathrust earthquake have temporarily increased the seismic hazards in the southeastern peninsula.

KEY POINTS

- Probabilistic seismic hazard analysis results for the Korean Peninsula are presented.
- The northwestern, south-central, and southeastern peninsula present relatively high-seismic hazard potentials.
- Recent moderate-size earthquakes increased the seismic hazard potentials in the southeastern peninsula.

INTRODUCTION

The Korean Peninsula is located in the eastern Eurasian plate that composes a stable intraplate environment with relatively low seismicity (e.g., Hong *et al.*, 2015). Historical earthquake records demonstrate the potential for damaging earthquakes to occur (e.g., Lee and Yang, 2006; Korea Meteorological Administration, 2012; Houng and Hong, 2013; Hong, Park, and Houng, 2016). Recent moderate-size earthquakes, including the 12 September 2016 M_L 5.8 Gyeongju earthquake and the 15 November 2017 M_L 5.4 Pohang earthquake, raised concerns on seismic hazards in the peninsula (Hong *et al.*, 2017, 2018).

Earthquake occurrence rates and ground motions are major factors that control the level of seismic hazards in a region. The earthquake occurrence in a certain region is dependent on seismic and geophysical environments, including medium properties, stress field, and fault structure, causing difficulty to apply the deterministic approach for seismic hazard assessment.

Probabilistic seismic hazard analysis (PSHA) was introduced to calculate the levels of ground motions for given time periods in a probabilistic sense, considering the source and medium effects (Cornell, 1968; Baker, 2008; Fujiwara *et al.*, 2009; Petersen *et al.*, 2014). The PSHA considers the seismic source activity as a random process in time and space, satisfying the observed earthquake occurrence statistics (Cornell, 1968; Fujiwara *et al.*, 2009). The PSHA is adopted globally and is periodically updated to reflect the latest observations and seismic models (e.g., Fujiwara *et al.*, 2009; Petersen *et al.*, 2014; Woessner *et al.*, 2015).

There were studies on seismic hazard assessment for neighboring regions that include Japan, China, Taiwan, and northern Eurasia (Ulomov and the GSHAP Region 7 Working Group, 1999; Fujiwara *et al.*, 2009; Miyazawa and Mori, 2009; Liu *et al.*, 2013; Wang *et al.*, 2016; Rong *et al.*, 2020). In addition, there were efforts to perform a seismic hazard analysis for the Korean Peninsula last decades (Ministry of Construction and Transportation, 1997; National Emergency

1. Department of Earth System Sciences, Yonsei University, Seoul, South Korea, https://orcid.org/0000-0002-8652-3229 (SP); https://orcid.org/0000-0002-3667-5005 (T-KH)

*Corresponding author: tkhong@yonsei.ac.kr

Cite this article as Park, S., T.-K. Hong, and G. Rah (2021). Seismic Hazard Assessment for the Korean Peninsula, *Bull. Seismol. Soc. Am.* **111**, 2696–2719, doi: 10.1785/0120200261

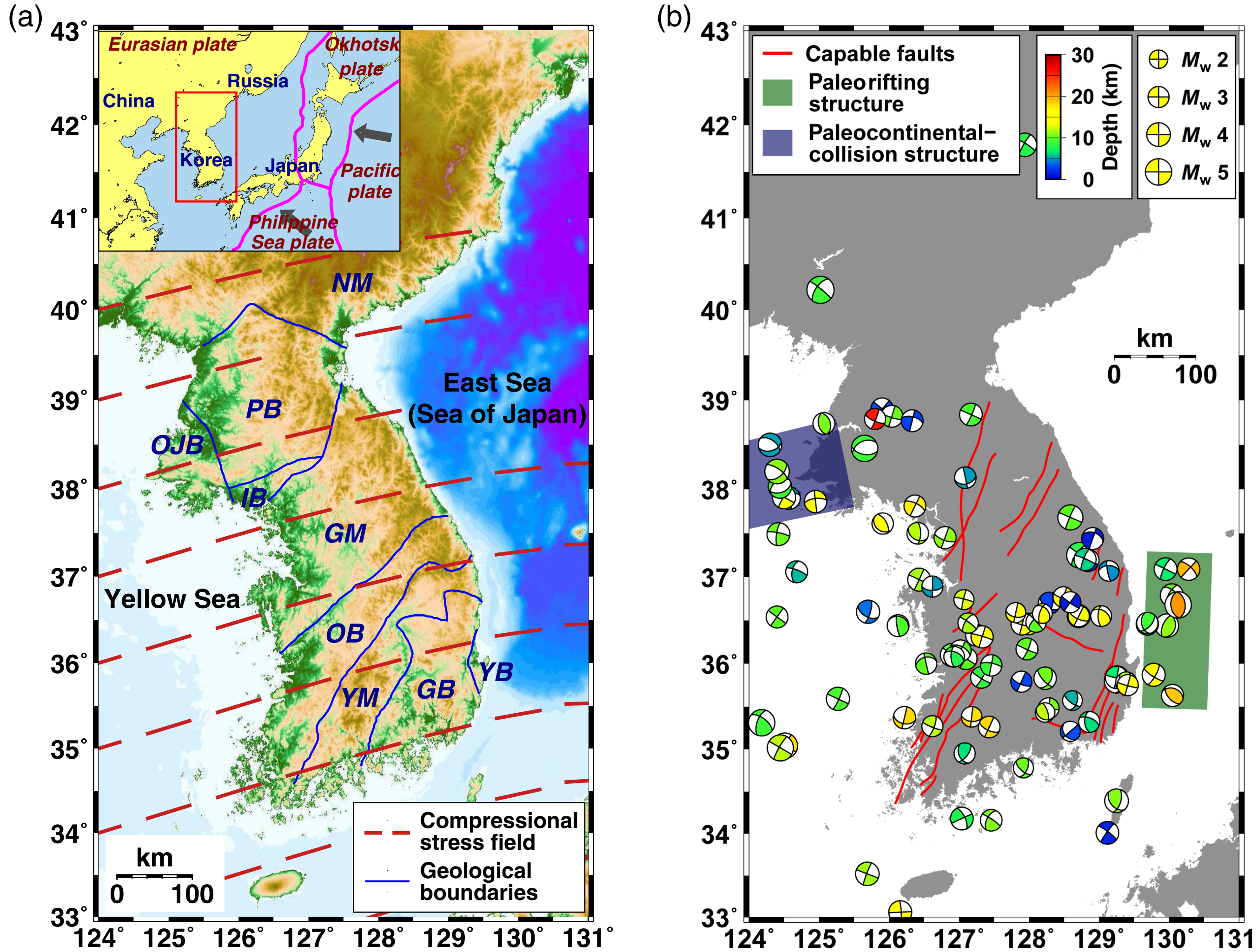

Figure 1. (a) Geological and tectonic settings around the Korean Peninsula. Major geological provinces (solid lines) are presented: GB, Gyeongsang basin; GM, Gyeonggi massif; IB, Imjingang belt; NM, Nangrim massif; OJB, Ongjin basin; OB, Okcheon belt; PB, Pyeongnam basin; YB, Yeonil basin; YM, Yeongnam massif. The orientation of the primary compressional field inferred from focal mechanism solutions is indicated with bars (Lee *et al.*, 2017). The study area is marked in the inset. (b) Major surface faults and focal mechanism solutions of earthquakes. The major surface faults (solid lines) and paleo-tectonic structures (shaded) are denoted (Choi, Hong, *et al.*, 2012; Hong and Choi, 2012; National Emergency Management Agency, 2012). The color version of this figure is available only in the electronic edition.

Management Agency, 2012, 2013; Kyung *et al.*, 2016). However, previous studies suffer from limited data and input parameter accuracy. Input parameters and models could not be fully verified for field observations. Recent advances in available data sets and seismic models may allow us to perform a PSHA for the Korean Peninsula. The seismic hazard analysis for the Korean Peninsula may complete the seismic hazard assessment of eastern Asia.

In particular, there was a noticeable increase in seismicity, including moderate-size earthquakes and earthquake tremors in the Korean Peninsula since the 11 March 2011 M_w 9.0 Tohoku–Oki megathrust earthquake (Hong *et al.*, 2015, 2018; Hong, Park, *et al.*, 2020). The recent seismicity properties should be reflected properly.

We perform a PSHA for the Korean Peninsula with implementation of up-to-date observations, earthquake parameters, and ground-motion models, presenting an updated seismic hazard model. The area source models are constructed based on the instrumental and historical earthquake records. Ground-motion prediction equations (GMPEs) from recent studies are calibrated against the observed ground motions. We carry out the PSHA for seismotectonic province models and ground-motion attenuation equations in the logic-tree scheme. We assess the sensitivity of each model with respect to the results.

GEOLOGY AND SEISMICITY

The Korean Peninsula is located in the eastern Eurasian plate, ~1400 km away from the plate boundaries off the eastern

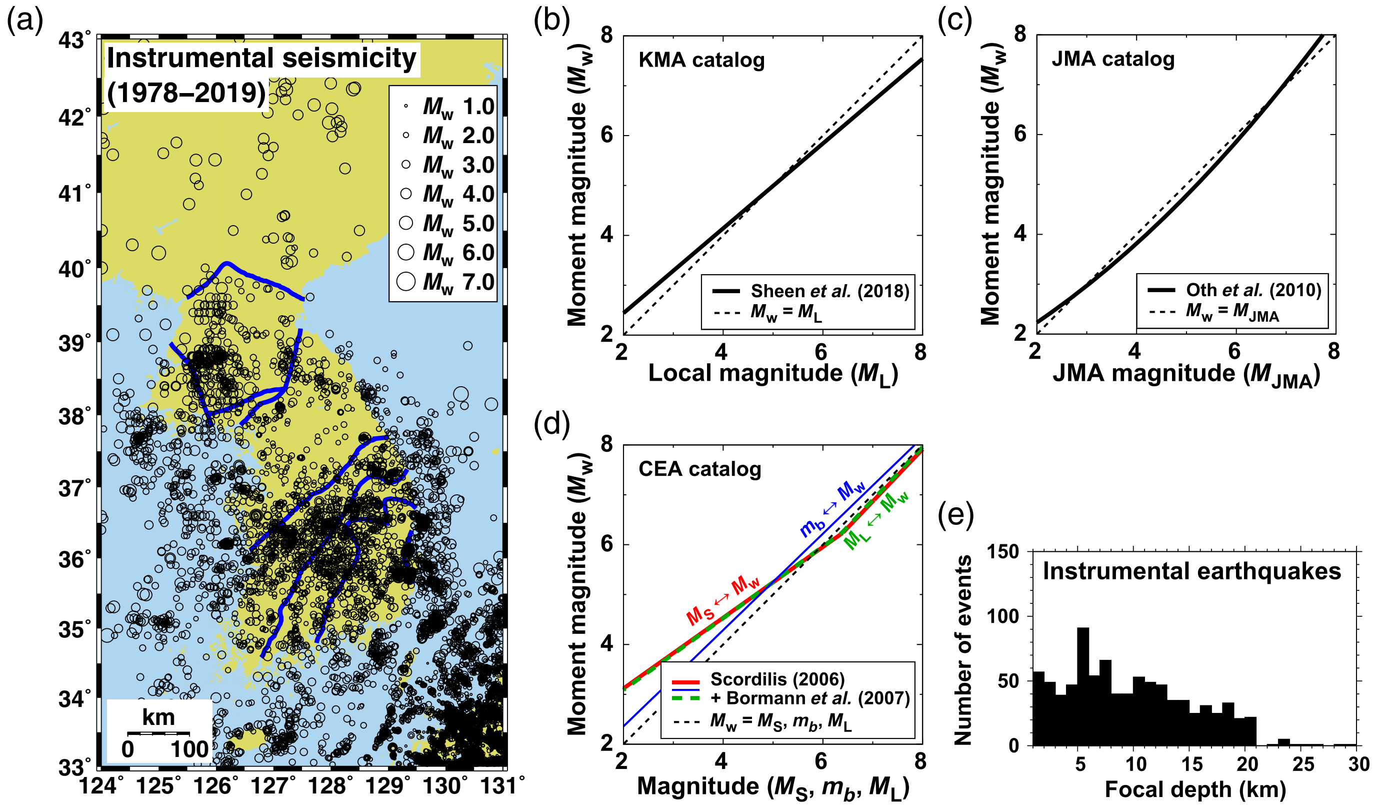

Figure 2. (a) Instrumental seismicity around the Korean Peninsula during 1978–2019. Earthquake catalogs of the Korea Meteorological Administration (KMA), Japan Meteorological Agency (JMA), and China Earthquake Administration (CEA) are combined. Relationships between the moment magnitude scale and magnitude scales in the (b) KMA, (c) JMA, and (d) CEA earthquake catalogs (Scordilis, 2006; Bormann *et al.*, 2007; Oth *et al.*, 2010; Sheen *et al.*, 2018). (e) Focal depth distribution of instrumental earthquakes (Hong, Park, and Houng, 2016). Most focal depths are less than 20 km. The color version of this figure is available only in the electronic edition.

Japanese islands (Fig. 1). The peninsula experienced multiple tectonic evolutions, including continental collisions and rifting that constructed complex geological structures with three Precambrian massif blocks (Nangrim, Gyeonggi, and Yeongnam), two intervening fold belts (Imjingang and Okcheon), and sedimentary basins of the late Proterozoic to Phanerozoic and Cretaceous periods (Pyeongnam and Gyeongsang basins) (Chough *et al.*, 2000) (Fig. 1). The East Sea (Sea of Japan) was opened by continental rifting during the Oligocene to mid-Miocene (Jolivet *et al.*, 1994).

The complex geological structures lead to strong lateral variations in medium properties, including the densities, seismic velocities, and seismic amplification and attenuation (e.g., Cho *et al.*, 1997; Hong and Kang, 2009; Hong, 2010; Hong and Lee, 2012; Jo and Hong, 2013). We observe relatively high-mantle-lid *P* velocities and low-crustal seismic attenuation in the central Korean Peninsula. The southern Korean Peninsula presents relatively low-mantle-lid *P* velocities, low-crustal *S* velocities, and large crustal attenuation.

The East Sea presents transitional structures between continental and oceanic crusts (Cho *et al.*, 2004; Hong, Park, and Houng, 2016). On the other hand, the inland peninsula and Yellow Sea have continental crusts. The crustal thicknesses are 28–38 km in the peninsula and 8.5–14 km in the East Sea (Hong *et al.*, 2008; Choi, Hong, *et al.*, 2012). The crust in the East Sea presents relatively low-seismic velocities (Hong *et al.*, 2008; Hong and Kang, 2009).

The Korean Peninsula is in an east-northeast–west-southwest compressional stress field that is mainly originated from the convergent boundaries with the Pacific and Philippine Sea Plates off the Japanese islands (Choi, Hong, *et al.*, 2012; Lee *et al.*, 2017) (Fig. 1). The seismicity around the peninsula is low. Strike-slip events are dominant in the peninsula (Hong and Choi, 2012; Lee *et al.*, 2017) (Fig. 1). Reverse- and normal-faulting events occur in the eastern and western offshore regions. Some reverse- and normal-faulting events are associated with the reactivation of paleotectonic structures (Choi, Hong, *et al.*, 2012; Hong and Choi, 2012) (Fig. 1).

The seismicity rates are relatively high in the northwestern and southern Korean Peninsula (Okcheon belt, Yeongnam massif, Pyeongnam basin, and Gyeongsang basin) and the southeastern offshore region (Fig. 2). The seismicity rates are relatively low in the central and northern Korean Peninsula (Nangrim massif and Gyeonggi massif) (Houng and Hong,

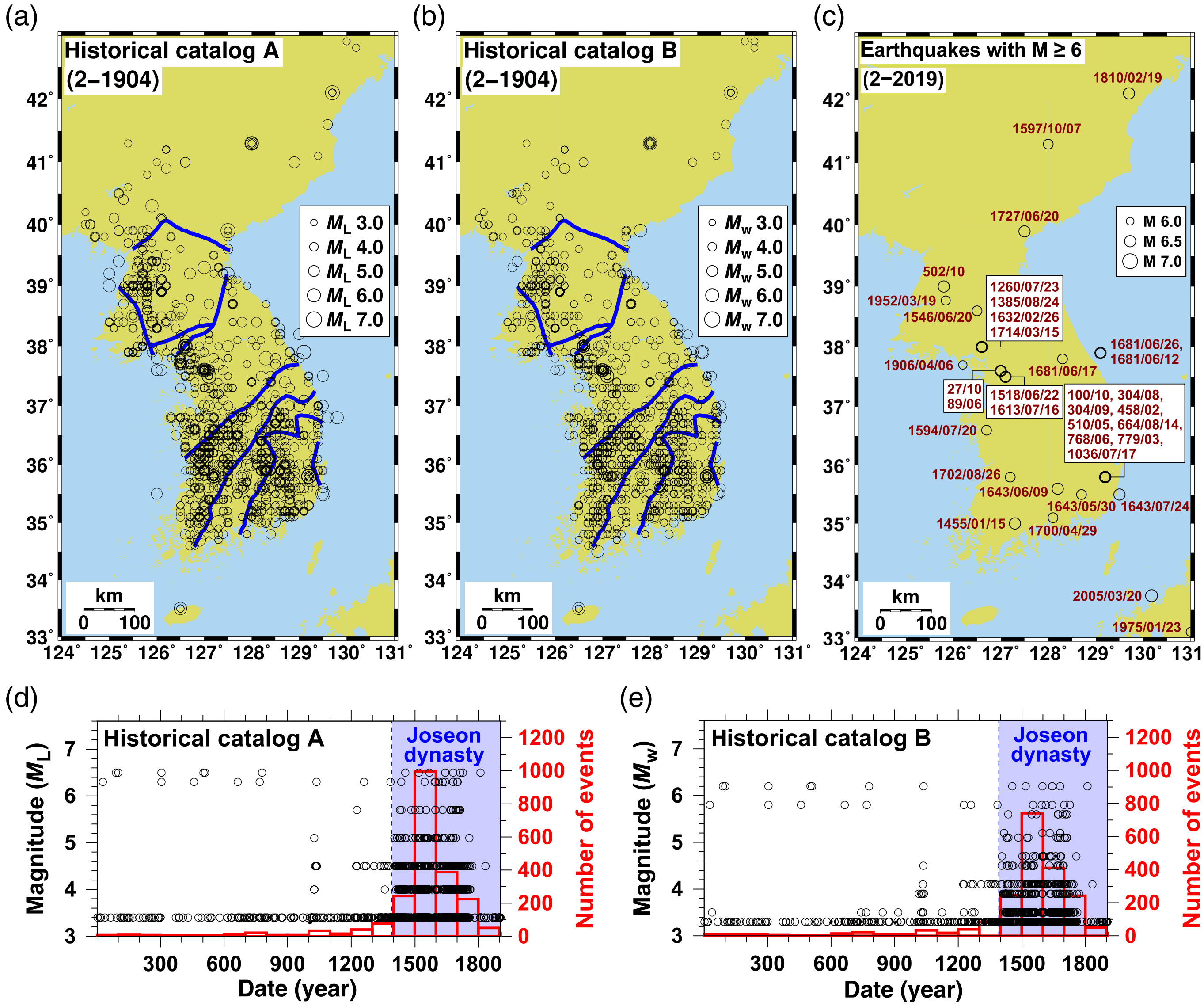

Figure 3. Historical seismicity around the Korean Peninsula during 2-1904: historical catalogs (a) A and (b) B. The historical seismicity is high in the northwestern and southern Korean Peninsula. (c) Spatial distribution of historical earthquakes with magnitudes of 6. The event dates (year/month/day) are presented. Temporal distribution of historical earthquakes for historical catalogs (d) A and (e) B. The numbers of historical earthquakes in every 100 yr are presented with histograms. The historical earthquakes were relatively well recorded during the Joseon dynasty (shaded period). The color version of this figure is available only in the electronic edition.

2013; Hong, Park, and Houng, 2016). The largest earthquake since 1978, when the national earthquake monitoring began, is the 12 September 2016 M_L 5.8 (M_w 5.4) earthquake (Hong *et al.*, 2017). There were earthquakes with magnitudes greater than M_w 6.0 in the offshore regions before 1978 (Jun and Jeon, 2001, 2010; Hong, Park, Lee, and Kim, 2020).

Historical seismic-damage records are a primary resource to present the information on the earthquakes in the preinstrumental era (Fig. 3). The historical seismic-damage records offer a unique opportunity to infer the long-term seismicity in regions where active faults are hardly identified on the surface. The historical earthquakes are highly distributed in the northwestern and southern Korean Peninsula, which is consistent with the instrumental seismicity. There might be earthquakes with magnitudes as large as $M_L \sim 7$, according to the historical earthquake records (Lee and Yang, 2006; Houng and Hong, 2013; Hong, Park, and Houng, 2016) (Fig. 3).

There are Quaternary faults found on the surface (e.g., Lee and Henry, 2001; Kyung and Lee, 2006; Choi, Chwae, *et al.*, 2012) (Fig. 1). However, there are no faults with full information including fault dimension, geometry, slip rate, slip displacement, recurrence time interval, and the most recent activation time (Lee and Henry, 2001; Kyung and Lee, 2006; National Emergency Management Agency, 2012).

METHODS

Seismicity varies with regional properties including fault structure, and local and regional stress fields (e.g., Gerstenberger *et al.*, 2001; Khan *et al.*, 2011; Lee and Hong, 2014). Seismotectonic provinces define the areas where uniform seismicity and tectonic activities are expected (e.g., Cornell, 1968; Secanell *et al.*, 2004; Musson, 2012; Stirling *et al.*, 2012; Petersen *et al.*, 2014; Hong, Park, and Houng, 2016). We measure the seismicity rates by seismotectonic province (e.g., Cornell, 1968; Woessner *et al.*, 2015; Hong, Park, and Houng, 2016). We calculate smoothed seismicity rates to complement the seismotectonic province-based seismicity rates (Frankel, 1995; Fujiwara *et al.*, 2009; Houng and Hong, 2013).

The seismicity rate per unit area in seismotectonic province k for earthquakes with magnitudes $\geq m$, $\lambda_k^p(m)$ is given by

$$\lambda_k^p(m) = \frac{q_k(m)}{TS_k}, \quad (1)$$

in which $q_k(m)$ is the number of earthquakes with magnitudes $\geq m$ in seismotectonic province k, T is the observation period, and S_k is the area of seismotectonic province k. The study region is discretized by uniform-size cells. The smoothed seismicity rate per unit area for earthquakes with magnitudes $\geq m$ at discretized cell i ($\lambda_i^s(m)$) is given by (Frankel, 1995; Houng and Hong, 2013):

$$\lambda_i^s(m) = \frac{\sum_{j=1}^{N} n_j(m)\exp[-l_{ij}^2/(2\sigma_l^2)]}{A_i T \sum_{j=1}^{N}\exp[-l_{ij}^2/(2\sigma_l^2)]}, \quad (2)$$

in which N is the total number of cells, $n_j(m)$ is the number of earthquakes with magnitudes $\geq m$ at cell j, l_{ij} is the distance between cells i and j, A_i is the area of cell i, and σ_l is the smoothing distance.

The seismotectonic province-based seismicity rates, smoothed seismicity rates, and whole-region average seismicity rate are combined into representative seismicity rates (Fujiwara *et al.*, 2015):

$$\lambda_i^r(m) = v_p\lambda_{z(i)}^p(m) + v_s\lambda_i^s(m) + v_u\lambda^u(m), \quad (3)$$

in which $\lambda_i^r(m)$ is the representative seismicity rate per unit area for earthquakes with magnitudes $\geq m$ at cell i, $z(i)$ is the seismotectonic province of cell i, $\lambda^u(m)$ is the whole-region average seismicity rate for earthquakes of magnitudes $\geq m$, and v_p, v_s, and v_u are weights satisfying $v_p + v_s + v_u = 1$.

Earthquakes satisfy the Gutenberg–Richter magnitude–frequency relationship (Gutenberg and Richter, 1956):

$$F(m) = 10^{a-bm}, \quad (4)$$

in which $F(m)$ is the number of earthquakes with magnitudes $\geq m$, and a and b are constants. The probability density function of event magnitudes $f(m)$ is given by (Kijko and Singh, 2011):

$$f(m) = \frac{\ln(10)\times b\times 10^{-bm}}{10^{-bm_{\min}} - 10^{-bm_{\max}}}, \quad (5)$$

in which $m_{\min}$ is the minimum magnitude and $m_{\max}$ is the maximum magnitude.

We determine the Gutenberg–Richter b-value using the maximum-likelihood method that yields stable estimates for catalogs with exceptional earthquakes and substantial magnitude errors (Bender, 1983; Marzocchi and Sandri, 2009). The conventional least-squares-fitting method may suffer from unstable b estimation for incomplete catalogs (e.g., Bender, 1983; Marzocchi and Sandri, 2009; Han *et al.*, 2015; Roberts *et al.*, 2015).

The amplitude of earthquake ground motion increases with the earthquake magnitude and decreases with distance. The GMPE is generally given by (e.g., Atkinson and Boore, 2006; Hong, Choi, *et al.*, 2016; Zhao *et al.*, 2016):

$$\log Y(m,h,l) = C(m) - D(m,h,l) + \epsilon, \quad (6)$$

in which $Y(m,h,l)$ is the ground-motion amplitude at epicentral distance l for an earthquake with magnitude m and focal depth h, $C(m)$ is the magnitude-dependent amplitude calibration term, $D(m,h,l)$ is the distance-dependent attenuation term, and ϵ is the local-perturbation term associated with the source, ray path, and receiver site. The amplitude perturbations follow the Gaussian distribution with zero mean and standard deviation σ_Y (e.g., Bender and Perkins, 1993; Atkinson and Boore, 2006; Pezeshk *et al.*, 2011).

For a given set of source and receiver, the probability of ground-motion amplitude to be exceeding a prescribed level by the local perturbation is

$$\begin{aligned} e(m,h,l) &= P(Y > y|m,h,l,\epsilon) \\ &= \frac{1}{\sqrt{2\pi}\sigma_Y}\int_{\log(y)}^{\infty}\exp\left[-\frac{\{z-\log(Y(m,h,l))\}^2}{2\sigma_Y^2}\right]dz, \end{aligned} \quad (7)$$

in which y is the prescribed ground-motion amplitude, and σ_Y is the standard deviation of the local-perturbation term (ϵ).

We calculate ground-motion amplitudes induced by point sources that occur independently. The locations of points sources are distributed homogeneously in discretized seismotectonic provinces. Here, the occurrence frequency of ground-motion amplitude exceeding y at a site k $\gamma_k(y)$ is given by (Cornell, 1968; Fujiwara *et al.*, 2009):

$$\gamma_k(y) = \sum_{c=1}^{N_s} A_c\lambda_c^r(m_{\min}^c)\int_{m_{\min}^c}^{m_{\max}^c} e(m,h^c,l_{kc})f(m|b_c)dm, \quad (8)$$

in which N_s is the number of point sources in discretized domain, A_c is the area of source c, h^c is the focal depth of source c, $m_{\min}^c$ and $m_{\max}^c$ are the minimum and maximum magnitude of source c, and b_c is the b-value of source c.

The Poisson-distribution probability of ground-motion amplitude Y exceeding y at site k in time period τ, $D_k^\tau(y)$, is given by

$$D_k^\tau(y) = P(Y > y) = 1 - \exp(-\gamma_k \tau). \quad (9)$$

The probability function combining the results for given sets of model parameters is given by

$$R_k^\tau(y) = \sum_i^{N_m} D_k^\tau(y|H_i)w_i = \sum_i^{N_m} [P(Y > y|H_i)]w_i, \quad (10)$$

in which $R_k^\tau(y)$ is the probability function combining the results for given sets of model parameters H_i at site k in time period τ, N_m is the number of model parameter sets, and w_i is the weight for the result of model parameter set H_i.

DATA

National seismic monitoring in the Korean Peninsula began in 1978 (Fig. 2). The instrumental earthquake catalogs for the Korean Peninsula and surrounding regions are available from the Korea Meteorological Administration (KMA), Japan Meteorological Agency (JMA), and China Earthquake Administration (CEA). We collect seismicity information for a region in 33° N–43° N and 124° E–131° E, since 1978. The earthquakes occurred in the crust. Deep-focus earthquakes with focal depths >400 km occur in the northeastern Korean Peninsula. We analyze the crustal events with focal depths <30 km for the seismic hazard assessment.

The earthquake catalog of KMA contains the information of 4170 events in 1978–2019, primarily covering the Korean Peninsula and offshore regions. The event magnitudes are 0.1–5.8 on the local magnitude scale (M_L). We additionally collect refined local magnitudes of 726 earthquakes from a previous work (Ministry of the Interior and Safety, 2019). The JMA earthquake catalog includes 59,583 earthquakes in 1978–2018, primarily covering the Japanese islands and surrounding regions. The magnitudes are from −1.3 to 7.0 on the JMA magnitude scale (M_{JMA}).

The CEA earthquake catalog includes 147 earthquakes in 1988–2019 that occurred in the northern Korean Peninsula, Yellow Sea, and eastern margin of China. The magnitudes (M_L, m_b, M_s) are 2.5–5.2. We also collect the moment magnitudes (M_w) of 56 earthquakes from the Global Centroid Moment Tensor project (see Data and Resources) and previous studies (Dziewonski *et al.*, 1981; Ekström *et al.*, 2012; Hong and Choi, 2012; Hong *et al.*, 2017, 2018).

We collect two historical earthquake catalogs in 2-1904 to supplement the instrumental seismicity information (Ministry of the Interior and Safety, 2019) (Fig. 3). The two historical earthquake catalogs were compiled based on available historical literatures (e.g., Samguksagi, Goryeosa, and Joseon–Wangjo–Sillok). The two historical catalogs were compiled independently with different felt-report interpretations and source-parameter inversions (Ministry of the Interior and Safety, 2019). Historical earthquake catalog A includes 2181 earthquakes with magnitudes between M_L 3.4 and 6.5. Historical earthquake catalog B includes 1981 earthquakes with magnitudes of M_w 3.3–6.2. Offshore historical earthquakes were recorded limitedly, because they produced small or rare seismic damages in inhabited regions.

The seismic waveforms are available from the KMA and Korea Institute of Geoscience and Mineral Resources (KIGAM). We collect 200 horizontal waveforms at stations on bedrock outcrops for three major earthquakes in the Korean Peninsula, including the 20 January 2007 M_L 4.5, 12 September 2016 M_L 5.8, and 15 November 2017 M_L 5.4 earthquakes.

REPRESENTATIVE EARTHQUAKE CATALOG

We assemble the instrumental earthquake catalogs of KMA, JMA, and CEA, producing a representative instrumental earthquake catalog (Fig. 2). We consider the events with origin time differences less than 20 s and distances less than 100 km for those in other catalogs to be duplicate events. We combine the earthquake catalogs with priority of KMA catalog against JMA and CEA catalogs for duplicate events. The magnitude scales are unified into the moment magnitude scale using magnitude-scale conversion relationships that are calibrated for the earthquake catalogs (Scordilis, 2006; Bormann *et al.*, 2007; Sheen *et al.*, 2018) (Fig. 2). The JMA magnitude scale is generally equivalent to the moment magnitude scale for shallow earthquakes (Katsumata, 1996; Oth *et al.*, 2010). We set the magnitudes on the JMA magnitude scale to be moment magnitudes.

The magnitude of completeness for the KMA catalog is M_L 2.5, which is equivalent to $M_w \sim 2.9$ (Houng and Hong, 2013; Hong *et al.*, 2015). The minimum magnitude of the JMA catalog to ensure the record completeness is $M_w \sim 1.6$ (Hong, Park, and Houng, 2016). The earthquake records of the CEA catalog cover the western margin of the study area, displaying apparent minimum magnitude of $M_w \sim 3.7$. The CEA catalog may be incomplete for small earthquakes in the Yellow Sea region. We compose a representative earthquake catalog combining all available KMA, JMA, and CEA catalogs.

The foreshocks and aftershocks of major earthquakes may be included in the instrumental earthquake catalogs. We remove the foreshocks and aftershocks from the earthquake catalogs to study the background seismicity (Marsan and Lengliné, 2008; Fujiwara *et al.*, 2009; Hong *et al.*, 2018). Conventional declustering methods are affected by spatiotemporal properties of aftershocks (Gardner and Knopoff, 1974; Reasenberg, 1985). However, the aftershock properties in the Korean Peninsula are poorly understood due to low seismicity. Nonparametric declustering methods are less affected by apparent variations in aftershock properties than the conventional methods (Marsan and Lengliné, 2008). We apply a

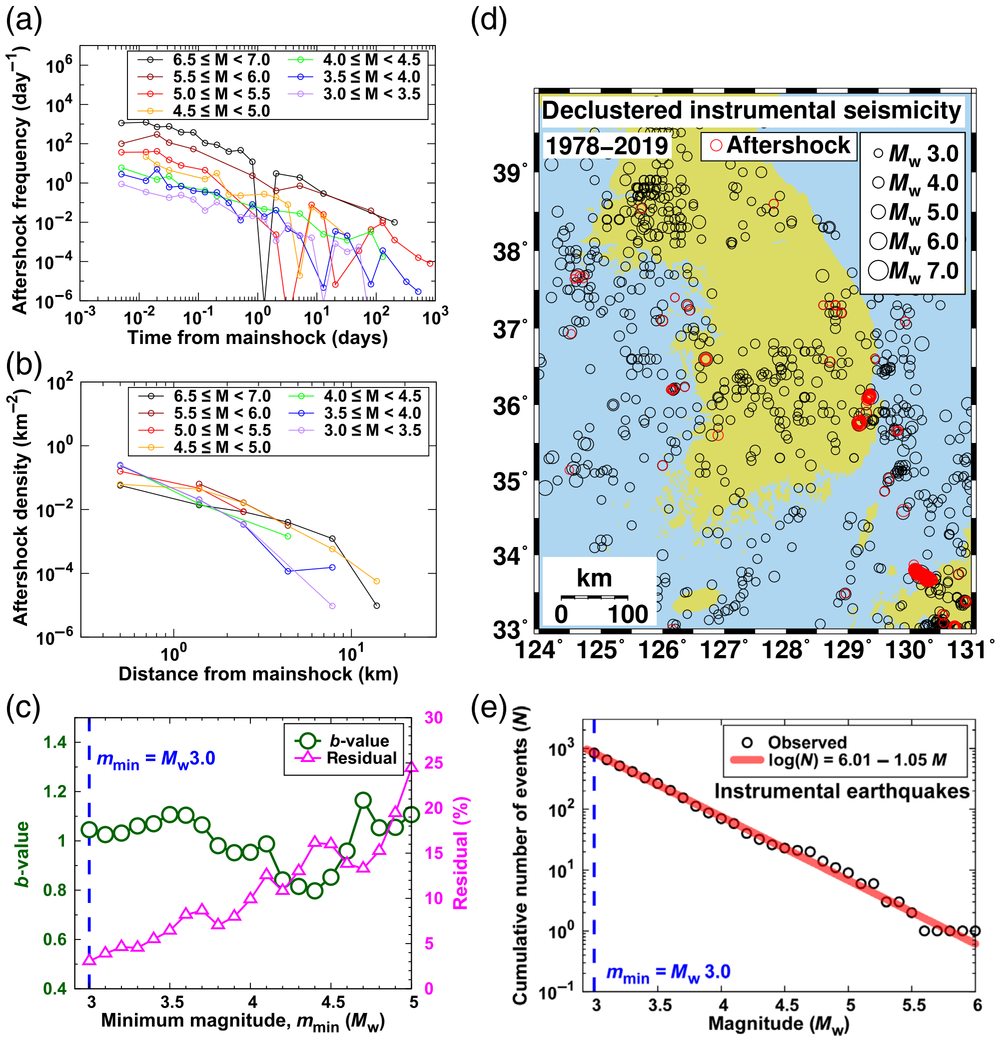

Figure 4. Declustering of instrumental seismicity and Gutenberg–Richter relationship. (a) Variation in aftershock occurrence frequency as a function of elapsed time since mainshock occurrence. Data points for discrete mainshock magnitude (M) bins are presented. The occurrence frequencies of aftershocks are proportional to the mainshock magnitudes, decaying with time. (b) Variation in spatial density of aftershock as a function of distance from mainshock. The aftershock densities generally decrease with the distance. (c) Declustered instrumental seismicity. The aftershocks are indicated. Assessment of declustered instrumental earthquake catalog: (d) variations in b-values (circles) and residuals between observed magnitude distribution and theoretical Gutenberg–Richter relationships (triangles) as a function of minimum magnitude, and (e) Gutenberg–Richter magnitude–frequency relationship for the declustered instrumental seismicity. The residual is less than 3% for m_{min} of M_w 3.0. The color version of this figure is available only in the electronic edition.

nonparametric declustering method to the instrumental earthquake records (Marsan and Lengliné, 2008). We decluster the instrumental earthquake records of magnitudes $M_w \geq 3.0$ (Fig. 4).

We sort the earthquakes in sequential order by origin time and interevent distance. We determine the temporal and spatial density functions of aftershocks based on the numbers of event pairs in discrete interevent times and distances (Fig. 4). The aftershock occurrence rates are proportional to the mainshock magnitudes. The aftershock occurrence rate decreases with time. The spatial densities of aftershocks are inversely proportional to the distances to the mainshocks. The features satisfy the typical aftershock properties (e.g., Utsu *et al.*, 1995; Marsan and Lengliné, 2008; Moradpour *et al.*, 2014; Hong *et al.*, 2017).

We group earthquake sequences considering the temporal and spatial densities of events. We consider the largest events in the earthquake sequences to be the mainshocks. We find 927 mainshocks. The foreshocks and aftershocks in the earthquake sequences are excluded in the hazard analysis.

We examine the completeness of the declustered earthquake catalog using a goodness-of-fit methods (Wiemer and Wyss, 2000). We determine the Gutenberg–Richter magnitude–frequency relationships for magnitude data points in 0.1 magnitude unit interval. We measure the residuals between the observed data points and theoretical fitted lines based on the Gutenberg–Richter relationship (Fig. 4). The residual is less than 3% for the minimum magnitude of M_w 3.0.

PROCEDURE

We assess the seismic hazards in rock sites by strong ground motions. The analysis procedure is largely divided into two steps. In the first step, we determine seismic model parameters including source models and GMPEs. In the second step, we perform sensitivity tests, validity tests, and PSHA.

We construct seismic source models based on the instrumental and historical earthquake catalogs. The accuracy and completeness are different between the instrumental and historical earthquake catalogs. Thus, the aggregation of the two catalogs may cause instability in the results (Weichert, 1980). We analyze the instrumental and historical earthquakes separately.

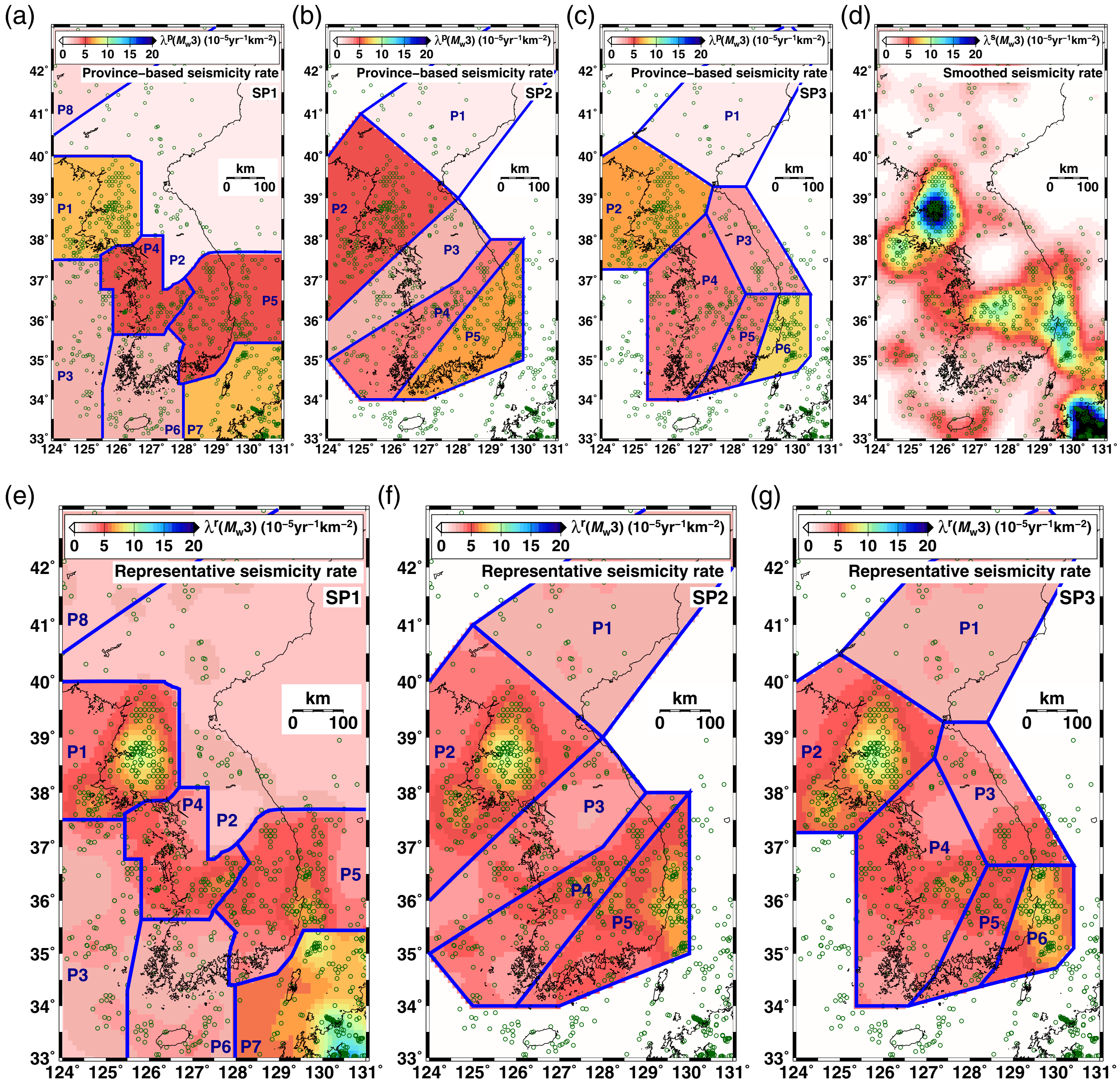

Figure 5. Seismicity rates for earthquakes with magnitudes $M_w \geq 3.0$. Seismicity rates (λ^p) by seismotectonic province models: (a) SP1, (b) SP2, and (c) SP3. The seismotectonic provinces are marked by solid lines. The epicenters of instrumental earthquakes are marked (open circles). (d) Spatially smoothed seismicity rates (λ^s). Representative seismicity rates (λ^r) combining the province-dependent seismicity rates and spatially smoothed seismicity rates: (e) SP1, (f) SP2, and (g) SP3. The color version of this figure is available only in the electronic edition.

The region in 33° N–43° N and 124° E–131° E is discretized into 0.1° × 0.1° cells for the analysis. The seismicity rates are determined based on the combined instrumental earthquake catalog. We determine the representative seismicity rate models based on the seismotectonic-province seismicity rates and smoothed seismicity rates. Historical earthquakes are not used for the seismicity rate models, considering the limited completeness and spatial coverage in earthquake catalogs.

We estimate the Gutenberg–Richter b-values for the instrumental and historical earthquakes using the maximum-likelihood method (Bender, 1983). We implement representative source depths and maximum magnitudes, considering the properties of major earthquakes in the Korean Peninsula. We collect GMPEs from previous studies. The equations are calibrated for the observed ground motions of major earthquakes. We construct a logic tree to manage epistemic uncertainties in seismic

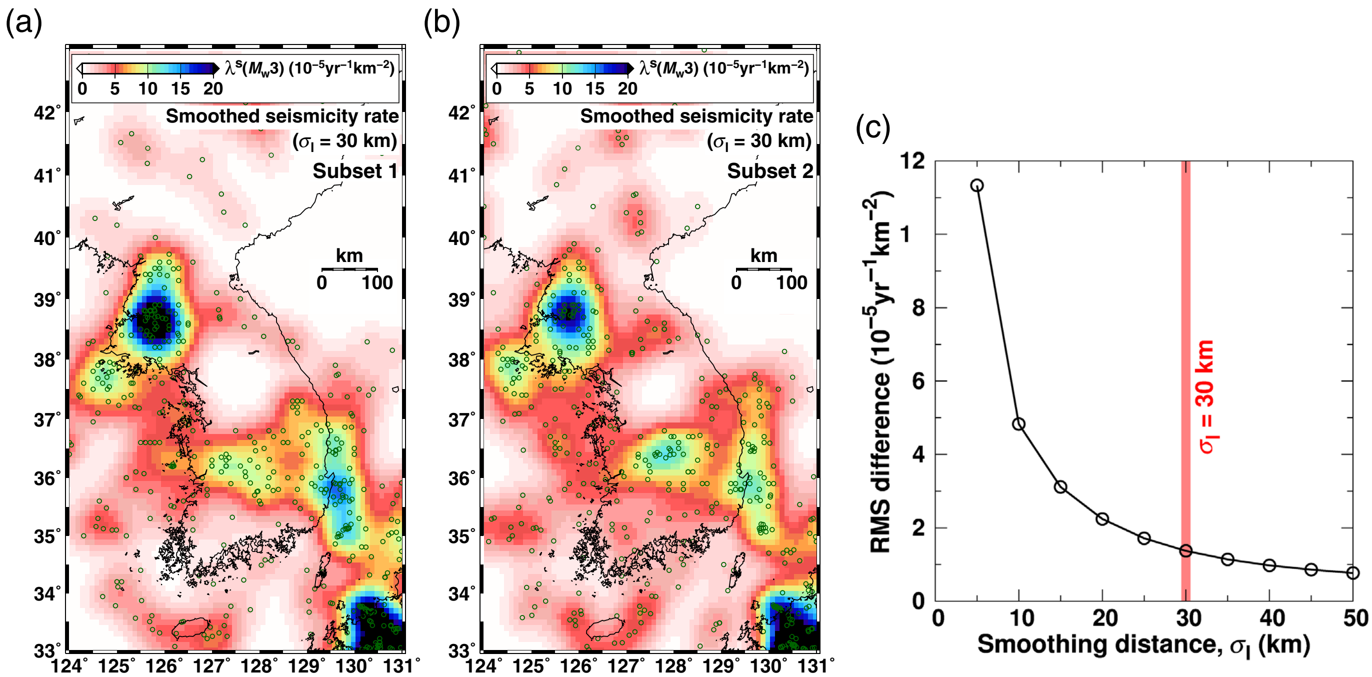

Figure 6. Stability test of smoothed seismicity rate models. Smoothed seismicity rate models based on (a) a half-earthquake data set and (b) the other earthquake data set. The smoothing distance (σ_l) is 30 km. (c) Variations in root mean square (rms) differences between the seismicity rate models as a function of smoothing distance. The case of $\sigma_l = 30$ km yields stable results. The color version of this figure is available only in the electronic edition.

models (Petersen *et al.*, 2014; Marzocchi *et al.*, 2015; Woessner *et al.*, 2015). We assign weights to the model parameters by considering the stabilities and errors associated with the model parameters.

We perform PSHA based on the logic tree. We consider point sources at discretized cells. The GMPEs are equally applied to every seismic sources. We examine the ground-motion level exceedance rates at every $0.1° \times 0.1°$ cell. We assess seismic hazards for a set of recurrence periods. Numerical codes are developed for PSHA. The codes and PSHA results are verified through benchmark tests and Monte Carlo ground-motion level simulation (Musson, 2012; Hale *et al.*, 2018). In addition, we examine the sensitivity of PSHA results to input model parameters.

INSTRUMENTAL SEISMICITY PROPERTIES

We collect seismotectonic province models from previous studies (Rhee *et al.*, 2012; Hong, Park, and Houng, 2016). Hong, Park, and Houng (2016) proposed a seismotectonic province model composed of seven seismotectonic provinces that cover the central and southern peninsula and oceanic regions. We modify the model to cover the whole Korean Peninsula and surrounding regions. The modified model is composed of eight seismotectonic provinces (Fig. 5a). Hereafter, we refer to the model to be SP1. We collect two models from Rhee *et al.* (2012). We set the models to be SP2 and SP3. The models cover the peninsula with some oceanic regions. Model SP2 is composed of five seismotectonic provinces, and model SP3 consists of six seismotectonic provinces (Fig. 5b,c).

We determine the seismicity rate model based on the representative instrumental earthquake catalog that is composed of KMA, JMA, and CEA catalogs since 1978. We calculate the seismotectonic province-based seismicity rate model for every seismotectonic province model (Fig. 5).

We calculate the smoothed seismicity rate model. Here, the smoothing distance may control the spatial distribution of smoothed seismicity rates. We determine the smoothing distance considering the event location error and seismicity distribution. We examine the effect of smoothing distance on the smoothed seismicity-rate distribution (Fig. 6). We divide the full instrumental earthquake data set into two subsets. Each subset is composed of earthquakes that are selected in every other earthquakes in the original full data set. We measure the root mean square (rms) differences between the seismicity rate models of the two subsets for smoothing distances between 5 and 100 km. The rms differences are small for smoothing distances $\geq \sim 30$ km, suggesting stable determination of seismicity rate models. We calculate the smoothed seismicity rate model with smoothing distance (σ_l) of 30 km (Fig. 5).

We determine the average seismicity rate for the whole peninsula (Fujiwara *et al.*, 2015). We combine the seismotectonic province-based seismicity rate model, smoothed seismicity rate model, and whole-peninsula average seismicity rate model to determine the representative seismicity rate model (Fig. 5). We reflect the influence of the whole-peninsula average seismicity

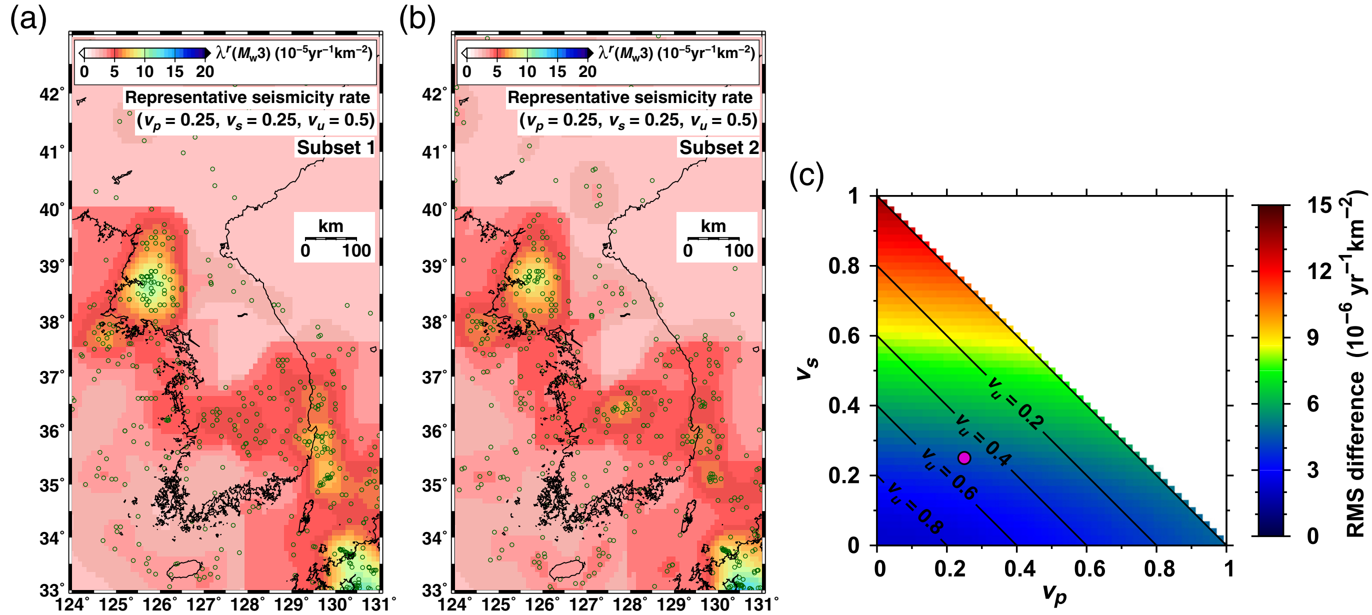

Figure 7. Stability test of the representative seismicity rate model based on two subsets. Seismicity rate models for (a) subset 1 and (b) subset 2. Weights for seismotectonic province-based seismicity rate model (v_p), smoothed seismicity rate model (v_s), and uniform seismicity rate model (v_u) are 0.25, 0.25, and 0.5, respectively. (c) Variations in rms differences between the seismicity rate models of two subsets as a function of weight. A set of weights with $v_p = 0.25$, $v_s = 0.25$, and $v_u = 0.5$ yields stable results (closed circle). The color version of this figure is available only in the electronic edition.

rate with weight of 0.5. We assign equal weights (0.25) to the seismotectonic province-based seismicity rate model and smoothed seismicity rate model.

We test the stability of the representative seismicity rate model. The instrumental earthquake catalog is divided into two subsets. We calculate the seismicity rate models based on the two data subsets with weights between 0 and 1. We examine the rms differences between the models from the subset data (Fig. 7). The rms differences are small for given

TABLE 1
Gutenberg–Richter Magnitude–Frequency Relationships for the Korean Peninsula

Earthquake Catalog	Seismotectonic Province Model	Province ID	Number of Earthquakes	*a*-Value	*b*-Value
Instrumental catalog	SP1	Whole region*	637	6.00 (± 0.13)	1.08 (± 0.04)
		P1	171	5.46 (± 0.25)	1.09 (± 0.08)
		P2	40	4.76 (± 0.50)	1.07 (± 0.17)
		P3	76	4.76 (± 0.33)	0.97 (± 0.11)
		P4	101	5.16 (± 0.31)	1.07 (± 0.11)
		P5	179	5.28 (± 0.23)	1.03 (± 0.08)
		P6	70	6.11 (± 0.51)	1.45 (± 0.17)
		P7	204	5.10 (± 0.20)	0.95 (± 0.07)
	SP2	Whole region*	590	5.99 (± 0.13)	1.09 (± 0.04)
		P2	209	5.51 (± 0.22)	1.08 (± 0.07)
		P3	82	4.99 (± 0.34)	1.04 (± 0.11)
		P4	127	5.22 (± 0.28)	1.05 (± 0.09)
		P5	172	5.55 (± 0.25)	1.12 (± 0.09)
	SP3	Whole region*	552	5.96 (± 0.14)	1.09 (± 0.04)
		P2	191	5.45 (± 0.23)	1.07 (± 0.08)
		P3	58	4.84 (± 0.40)	1.04 (± 0.14)
		P4	155	5.46 (± 0.26)	1.11 (± 0.09)
		P5	50	5.98 (± 0.61)	1.45 (± 0.21)
		P6	97	4.78 (± 0.28)	0.95 (± 0.10)
Historical catalog A	Entire Korean Peninsula		413	6.92 (± 0.21)	1.01 (± 0.05)
Historical catalog B	Entire Korean Peninsula		324	6.05 (± 0.20)	0.94 (± 0.05)

*Region in latitudes ≤40° N.

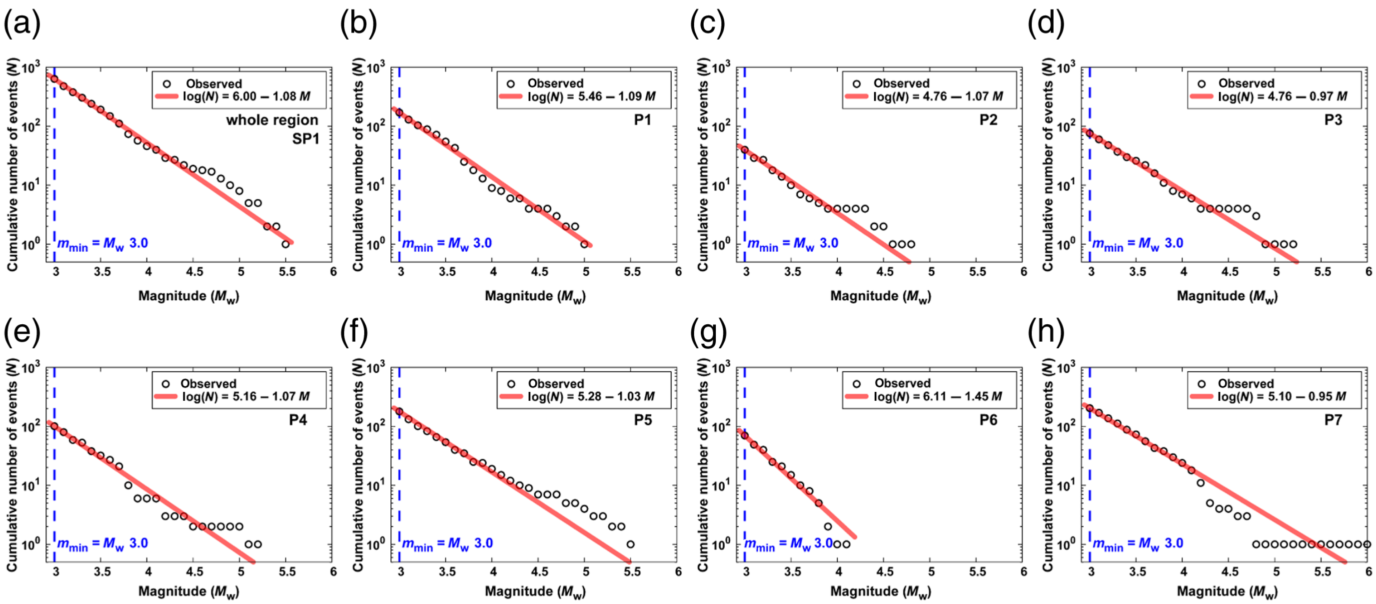

weights of $v_p = 0.25$, $v_s = 0.25$, and $v_u = 0.5$. The observation suggests the stability in seismicity rate models.

We determine the b-value for every seismotectonic province based on the representative earthquake catalog, excluding the earthquakes from the CEA catalog, to avoid possible distortion by catalog incompleteness. The b-values range between 0.95 and 1.13 for every seismotectonic province, except P6 of SP1 and P5 of SP2 (Table 1, Fig. 8). Each seismotectonic province has at least 40 earthquakes, except P8 of SP1, P1 of SP2, and P1 of SP3 (Fig. 5). The b-value estimates can be poorly constrained in regions with small seismic records. We implement the whole-peninsula b-value for the poorly constrained regions instead.

Figure 8. Gutenberg–Richter magnitude–frequency relationship of instrumental seismicity by seismotectonic province: (a) whole region, and (b) P1, (c) P2, (d) P3, (e) P4, (f) P5, (g) P6, and (h) P7 of model SP1. The theoretical Gutenberg–Richter relationships reasonably represent the observed magnitudes. The color version of this figure is available only in the electronic edition.

HISTORICAL EARTHQUAKE PROPERTIES

We analyze the historical earthquakes during the Joseon Dynasty in 1393–1904 that are most well recorded in historical periods (Houng and Hong, 2013). The spatial coverage of historical seismicity is poor compared to instrumental seismicity,

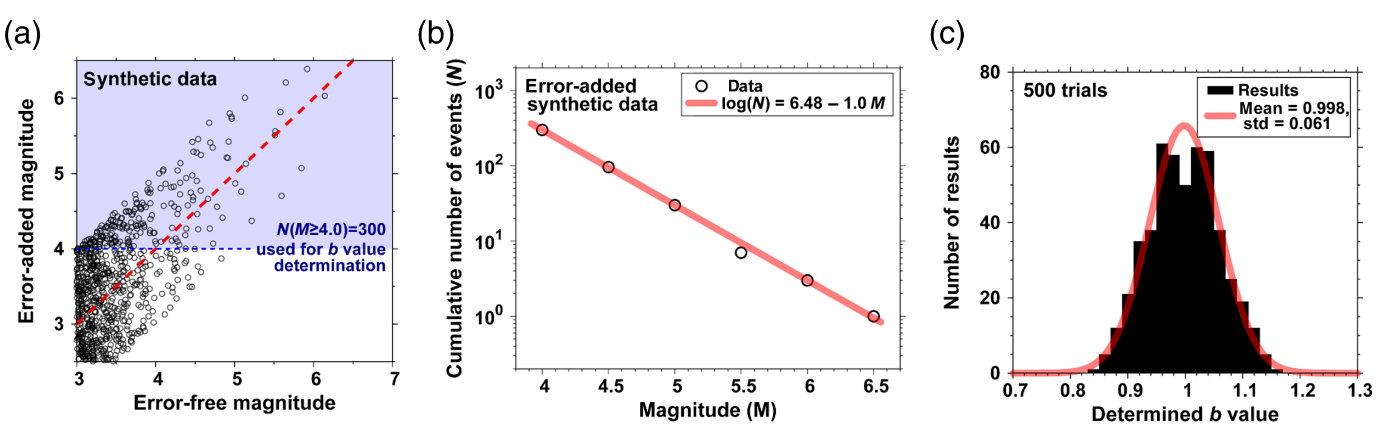

Figure 9. Validation test of b-value estimation for error-added magnitude data set. (a) Example of synthetic magnitude data set for b-value estimation. Random errors between −1 and 1 are added. Error-added magnitudes are compared with error-free magnitudes. The b-value is determined based on error-added magnitudes larger than or equal to 4.0. (b) Gutenberg–Richter relationship for the error-added synthetic data set. The estimated b-value is 1.0. (c) Distribution of b-value estimates for 500 synthetic magnitude data sets. The mean and standard deviation are 0.998 and 0.061, respectively. The color version of this figure is available only in the electronic edition.

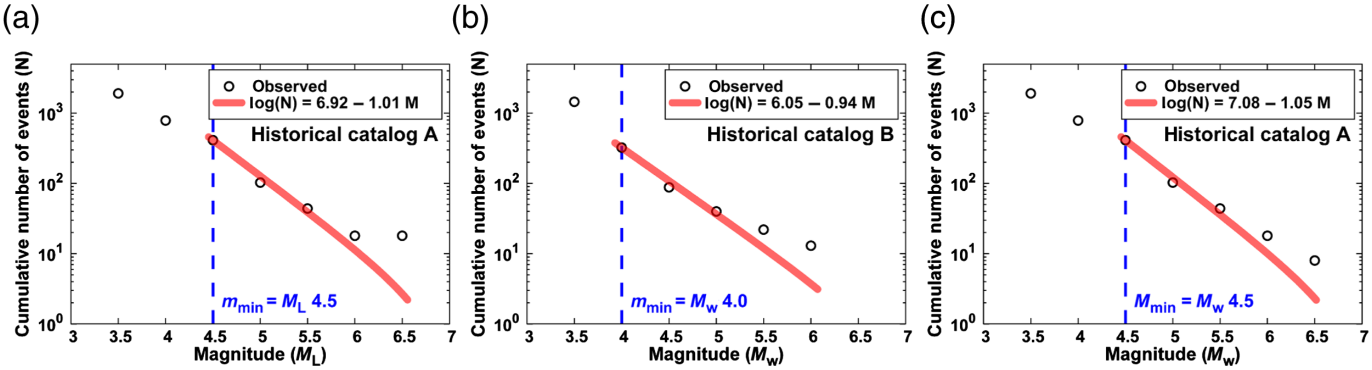

Figure 10. Gutenberg–Richter magnitude–frequency relationship of historical seismicity: (a) historical catalog A in local magnitude scale, (b) historical catalog B in moment magnitude scale, and (c) historical catalog A in moment magnitude scale. The minimum magnitudes for the catalogs are indicated. The color version of this figure is available only in the electronic edition.

which inhibits the analysis of historical earthquakes by seismotectonic province. We determine the representative b-value of historical seismicity for the whole peninsula. The magnitudes of historical earthquakes are sampled by 0.5 magnitude unit.

The historical earthquake magnitudes may have large uncertainty, which may cause instability in b-value estimation (Lee and Yang, 2006; Hough, 2013; Houng and Hong, 2013). We examine the validity in b estimates for magnitude data sets with large uncertainty. We produce 500 synthetic magnitude data sets that are composed of 300 magnitude data points. The magnitudes are randomly selected using the probabilistic distribution with b-value of 1.0. We add random errors between −1 and 1 to the magnitude data (Fig. 9a). The synthetic magnitude data are resampled by every 0.5 magnitude unit. We determine the b-values based on the data sets. (Fig. 9b). The estimated b-values have the mean of 0.998 and standard deviation of 0.061 (Fig. 9c). We find 90% of results to be between 0.9 and 1.1. The test suggests that the b-values can be reasonably determined based on historical earthquake catalogs under the assumption that historical magnitude estimates are not systematically biased, but only subject to random errors.

We jointly determine the b-value and minimum magnitude for the historical catalogs (Fig. 10). The residuals between the Gutenberg–Richter relationships and magnitude data points are examined. The residuals for the two historical catalogs are less than 10% at minimum magnitudes M_L 4.5 and M_w 4.0, respectively (Fig. 10a,b). The b-values at the minimum magnitudes are 1.01 and 0.94. Two historical catalogs present comparable b-values.

Historical catalog A presents the earthquake magnitudes on the local magnitude scale (M_L), whereas historical catalog B presents the earthquake magnitudes on the moment magnitude scale (M_w). When we convert the M_L magnitudes of historical catalog A to moment magnitudes using a magnitude-scale relationship (Sheen *et al.*, 2018), the estimated a- and b-values are close to those based on the local magnitude scale (Fig. 10c). It is known that the magnitudes for moderate-size earthquakes are comparable between the local magnitude scale and moment magnitude scale (Hong, 2012). Further, considering the inherent accuracy limitation in historical event magnitudes and possible error inclusion in magnitude-scaling conversion, we use the seismicity properties based on the local magnitude scale for seismic hazard analysis of historical catalog A for the PSHA.

GMPEs

The GMPE produces the expected ground-motion amplitudes for an earthquake of given magnitude as a function of distance. The equation may vary by region, depending on the medium properties and geology. We collect GMPEs for horizontal peak ground accelerations (PGAs) in the Korean Peninsula (Park *et al.*, 2001; Jo and Baag, 2003; Yun *et al.*, 2008; Emolo *et al.*, 2015; Korea Hydro and Nuclear Power, 2015; Hong, Choi, *et al.*, 2016) (Table 2). We refer the GMPE models to be GE1 for Park *et al.* (2001), GE2 for Jo and Baag (2003), GE3 for Yun *et al.* (2008), GE4 and GE5 for Korea Hydro and Nuclear Power (2015), GE6 for Emolo *et al.* (2015), and GE7 for Hong, Choi, *et al.* (2016).

Models GE1–GE5 are calibrated for the moment magnitude scale. Model GE6 was originally calibrated for the local magnitude scale (Emolo *et al.*, 2015). We covert model GE6 for moment magnitude scale, considering the calibration relationship between the local magnitude scale and moment magnitude scale (Choi *et al.*, 2004). Model GE7 was developed for a body-wave magnitude scale (Hong, Choi, *et al.*, 2016). Model GE7 is converted for the moment magnitude scale using a magnitude-scale relationship (Hong, Park, Lee, and Kim, 2020).

We calibrate the GMPEs for ground-motion amplitudes on rock sites. Models GE1–GE5 were developed based on synthetic ground motions on rock sites or bedrock outcrops. Models GE6 and GE7 were derived based on field observations on the surface. We calibrate models GE6 and GE7 for ground motions at bedrock for three major earthquakes that include the 20 January

TABLE 2
Ground-Motion Prediction Equations for the Korean Peninsula

Model	Equation	Data Coverage	Reference
GE1	$\log \mathrm{PGA} = c_0 + c_1 r - \log r$, $c_0 = 3.391 + 0.3601(M_w - 6) - 0.03621(M_w - 6)^2 - 6.385 \times 10^{-3}(M_w - 6)^3$ $c_1 = 10^{-5}[-366 + 126.7(M_w - 6) - 9(M_w - 6)^2 - 2.667(M_w - 6)^3]$	$10 \le r \le 350$, M_w 4.0–7.0	Park *et al.* (2001)
GE2	$\ln \mathrm{PGA} = c_0 + c_1 r + c_2 \ln(r) - \ln[\min(r, 100)] - \frac{1}{2}\ln[\max(r, 100)]$, $c_0 = 11.14645 + 0.5111930(M_w - 6) - 0.03853722(M_w - 6)^2 + 0.029179(M_w - 6)^3$ $c_1 = 10^{-5}[-243.8321 + 14.01897(M_w - 6) - 1.627163(M_w - 6)^2 + 5.987778(M_w - 6)^3]$ $c_2 = 10^{-3}[-321.4505 + 105.0434(M_w - 6) - 9.657898(M_w - 6)^2 - 6.503183(M_w - 6)^3]$	$10 \le r \le 500$, M_w 4.0–7.5	Jo and Baag (2003)
GE3	$\ln \mathrm{PGA} = 37.407 - 1.653M + (-6.5 + 0.474M_w) \ln(r + 199.14)$ $-0.065(M - 6)^2 - 1.101 \ln[\min(R, 50)] + 0.063 \ln[\max(R, 50)]$ $R = \begin{cases} \sqrt{r^2 + 9.8^2}, & \text{if } M_w \le 6.5 \\ \sqrt{r^2 + 9.8^2 \exp[-2.5 + 0.44(M_w - 1)]}, & \text{otherwise} \end{cases}$	$10 \le r \le 400$, M_w 4.0–7.0	Yun *et al.* (2008)
GE4	$\ln \mathrm{PGA} = c_0 + c_1 r + c_2 \ln(r) - \ln[\min(r, 100)] - \frac{1}{2}\ln[\max(r, 100)]$, $c_0 = 9.680528 + 0.5658149(M_w - 6) - 0.01418715(M_w - 6)^2 + 0.03129507(M_w - 6)^3$ $c_1 = 10^{-5}[-625.8455 + 33.08375(M_w - 6) - 9.772596(M_w - 6)^2 + 3.022639(M_w - 6)^3]$ $c_2 = 10^{-3}[-136.5383 + 81.73023(M_w - 6) - 17.83794(M_w - 6)^2 - 6.550721(M_w - 6)^3]$	$10 \le r \le 500$, M_w 4.0–7.0	Korea Hydro and Nuclear Power (2015)
GE5	$\ln \mathrm{PGA} = c_0 + c_1 r + c_2 \ln(r) - \ln[\min(r, 100)] - \frac{1}{2}\ln[\max(r, 100)]$, $c_0 = 10.34567 + 0.5693772(M_w - 6) - 0.02960611(M_w - 6)^2 + 0.03417921(M_w - 6)^3$ $c_1 = 10^{-5}[-634.3279 + 27.91516(M_w - 6) - 10.02967(M_w - 6)^2 + 4.284311(M_w - 6)^3]$ $c_2 = 10^{-3}[-154.4673 + 90.46445(M_w - 6) - 15.21858(M_w - 6)^2 - 7.448889(M_w - 6)^3]$	$10 \le r \le 500$, M_w 4.0–7.0	Korea Hydro and Nuclear Power (2015)
GE6*	$\log \mathrm{PGA} = -1.13 + 0.73M_w - 0.76 \log[\sqrt{l^2 + 1.7^2}] - 0.0029l$	$1.4 \le l \le 600$, M_w 2.0–4.9	Emolo *et al.* (2015)
GE7*	$\log \mathrm{PGA} = 1.244 + 0.528M_w - 1.44 \log r - 0.00211r$	$4 \le r \le 630$, M_w 4.0–5.9	Hong, Choi, *et al.* (2016)

l, epicentral distance (km); PGA, peak ground acceleration ($\mathrm{cm/s^2}$); r, hypocentral distance (km).
*Calibrated for observed peak ground accelerations at bedrock outcrops.

2007 M_w 4.5 earthquake, the 12 September 2016 M_w 5.4 earthquake, and the 15 November 2017 M_w 5.5 earthquake (Fig. 11).

The GMPEs reasonably match with the field observations in regional distances (Fig. 11). On the other hand, the GMPEs, except model GE7, appear to underestimate the ground motions in short distance. Model GE7 yields a reasonable match with field observations in both local and regional distances (Fig. 11). Model GE1 produces ground motions that decay rapidly in regional distance, presenting increasing deviations from field observations with distance (Fig. 11). Models GE2 and GE3 present comparable ground-motion levels in local distances. However, the ground-motion levels from model GE3 are slightly lower than those from model GE2 in regional distances. Model GE3 is better than model GE2 with respect to the overall fitness with field observations.

The ground-motion levels from models GE4 and GE5 present distance-dependent attenuation rates (Fig. 11). Model GE4 generally produces lower ground-motion levels than field observations. The overall fitness is better for model GE5 than for model GE4. Models developed from field observations appear to display better presentation of ground motions.

The standard deviations of GMPEs (σ_Y) represent the possible variations in ground-motion levels. Model-driven standard deviations may be dependent on the data quality that may vary by data set. The incorporation of model-dependent standard deviations may induce inconsistent perturbation in PSHA results (Bender and Perkins, 1993). The GMPEs in stable continental regions present standard deviations of 0.25–0.3 (Atkinson and Boore, 2006; Pezeshk *et al.*, 2011). The standard deviations of GMPEs in the Korean Peninsula are around 0.3 (Yun *et al.*, 2008). We apply a constant standard deviation of 0.26 to GMPEs, considering general applications in PSHA studies (Bender and Perkins, 1993).

LOGIC TREE

We consider alternative models and parameters of seismotectonic provinces, b-values, maximum magnitudes, source depths, and GMPEs through a logic tree (Fig. 12). We assign weights to models and parameters (Ministry of the Interior and Safety, 2019). The weights were assigned considering the data quality, data quantity, precision, and production year.

We consider three seismotectonic province models (Fig. 5). Seismotectonic province model SP1 covers both inland and oceanic regions in and around the Korean Peninsula. Models SP2 and SP3 mainly cover inland regions of the Korean Peninsula. Offshore events are poorly reflected in models SP2 and SP3. We assign weights to seismotectonic province models considering the regional coverage. We set the weights of 0.4, 0.3, and 0.3 to models SP1, SP2, and SP3, respectively (Fig. 12).

We consider three sets of b-values that include seismotectonic-province-dependent b-values for instrumental seismicity and two whole-region b-values for historical earthquakes (Fig. 12). We assign weights to b-values considering the numbers of data and catalog completeness. We assign a larger weight to the instrumental seismicity b-values relative to the historical seismicity b-

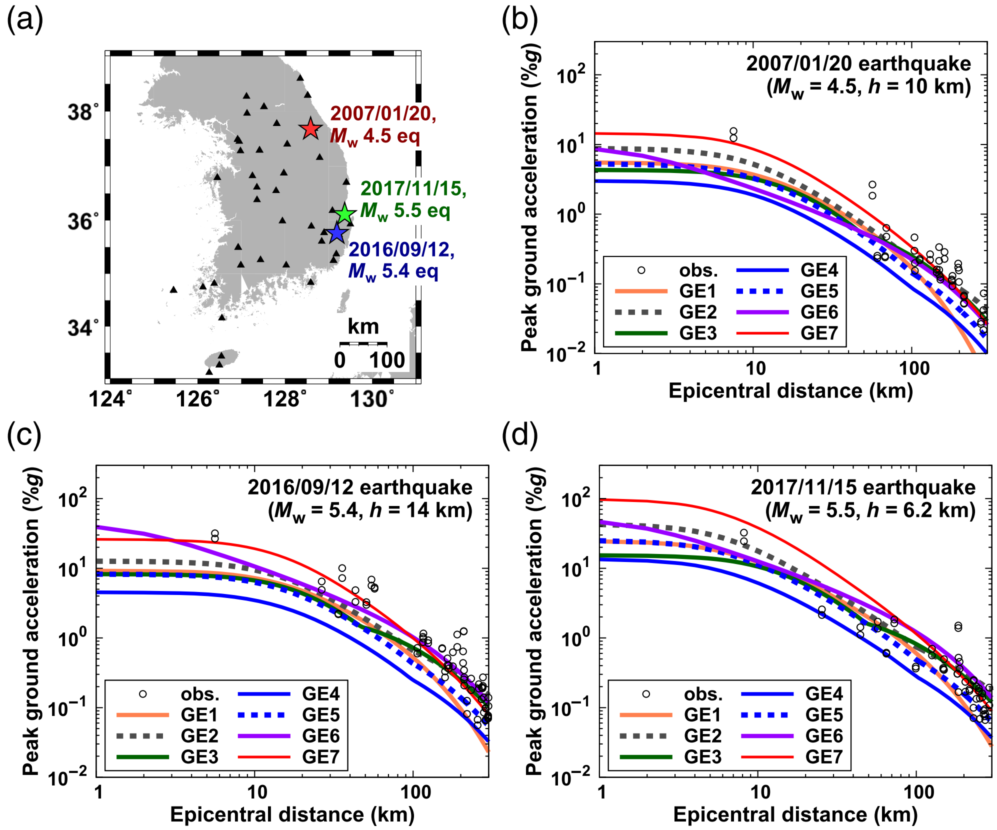

Figure 11. Comparison between ground-motion prediction equations (GMPEs) and observed amplitudes: (a) locations of earthquakes and stations, (b) the 20 January 2007 M_w 4.5 earthquake, (c) the 12 September 2016 M_w 5.4 earthquake, and (d) the 15 November 2017 M_w 5.5 earthquake. Model GE4 underestimates the ground-motion levels. The other GMPEs generally agree with the observed ground-motion levels. The color version of this figure is available only in the electronic edition.

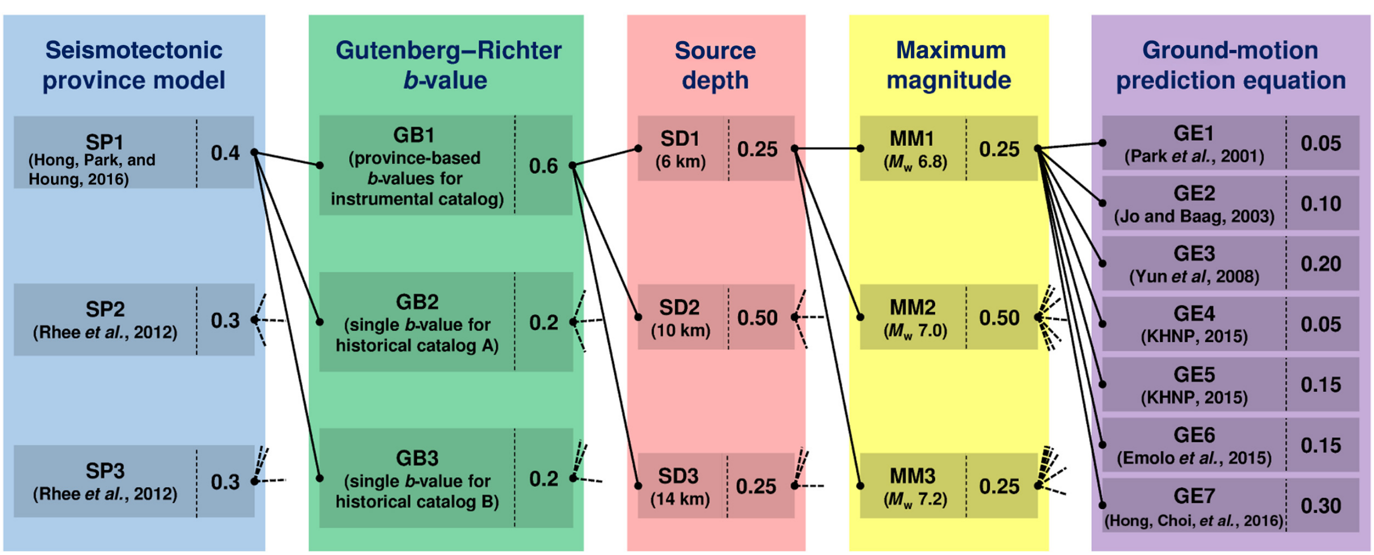

Figure 12. Logic tree of input model parameters with weights for probabilistic seismic hazard analysis (PSHA). The color version of this figure is available only in the electronic edition.

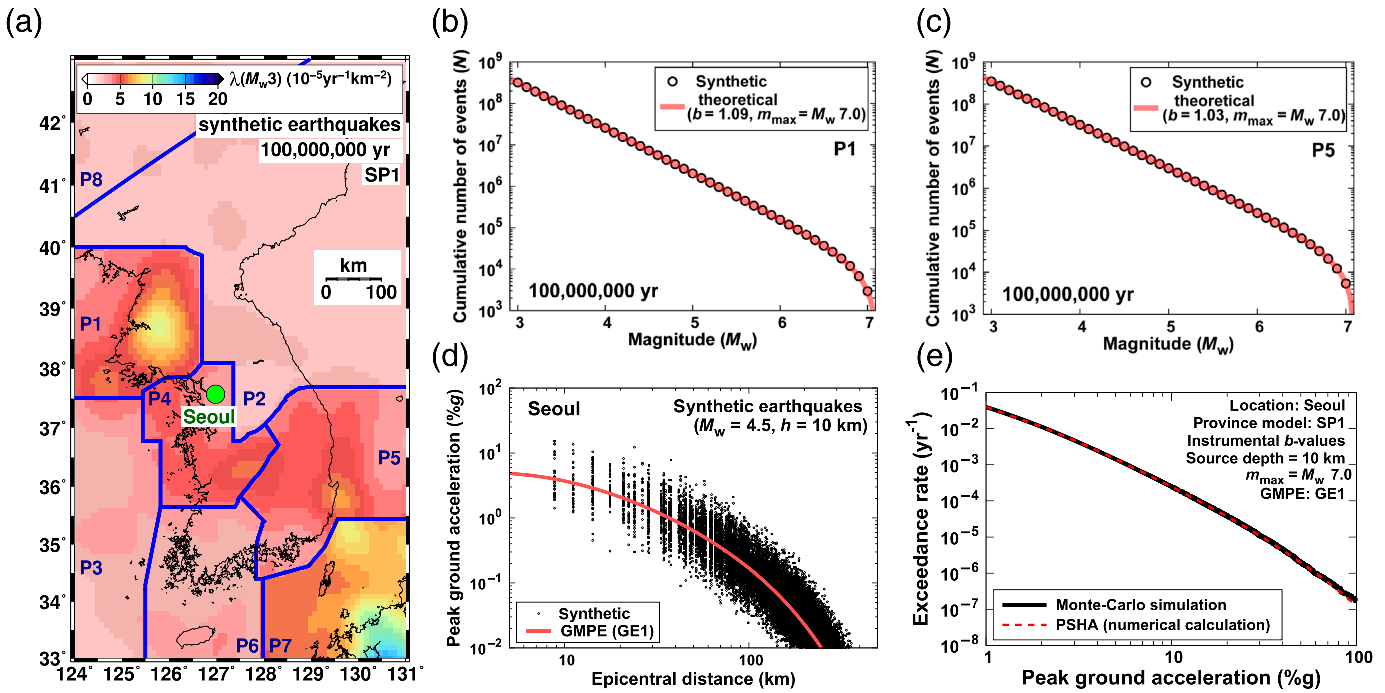

Figure 13. Validation test of PSHA using Monte Carlo simulation of earthquakes and ground-motion amplitudes: (a) seismicity rates (λ) of a synthetic earthquake catalog and cumulative magnitude distribution in the synthetic earthquake catalog for seismotectonic provinces (b) P1 and (c) P5. The synthetic earthquake catalog satisfies the theoretical Gutenberg–Richter relationship. (d) Variations in synthetic ground-motion amplitudes in Seoul for M_w 4.5 earthquakes as a function of epicentral distance. The synthetic ground-motion amplitudes are randomly perturbed from GMPE model GE1 (solid line). (e) Comparison between exceedance rates of ground-motion amplitudes in PSHA (dotted line) and Monte Carlo simulations (solid line). The color version of this figure is available only in the electronic edition.

values. The weights are 0.6, 0.2, and 0.2 for the instrumental seismicity b-values and two historical seismicity b-values (Fig. 12).

The source depth is a major parameter to control the ground-motion levels, particularly in short distances (Table 2) (Fig. 11). The focal depths are less than 20 km, mostly around 5–10 km, in and around the Korean Peninsula (Hong, Park, and Houng, 2016; Rachman and Chung, 2016; Chung *et al.*, 2018) (Figs. 1 and 2). We find that major earthquakes, including the 20 January 2007 M_w 4.5 earthquake, the 12 September 2016 M_w 5.4 earthquake, and the 15 November 2017 M_w 5.5 earthquake, occurred at depths ∼6–16 km (Choi, Hong, *et al.*, 2012; Hong *et al.*, 2017, 2018). We perform the PSHA for representative source depths of 6, 10, and 14 km. The logic tree combines the PSHA results with weights of 0.25, 0.5, and 0.25 (Fig. 12).

We determine the maximum magnitudes considering the paleoearthquake studies as well as the largest events in historical and instrumental earthquake catalogs. The historical and early-instrumental seismicity suggest that earthquakes with magnitudes **M** 6–7 occurred in and around the Korean Peninsula (Jun and Jeon, 2001, 2010; Lee and Yang, 2006; Houng and Hong, 2013) (Fig. 3). Geological studies suggest the potential earthquake magnitudes of $M_w \sim 7$ in the Korean Peninsula (Kyung, 2010). A probabilistic analysis suggests the maximum magnitude of $M_w \sim 7$ (Hong, Park, and Houng, 2016). A maximum magnitude $M_w \sim 7$ may be applicable to the Korean Peninsula, which is generally used in seismic hazard analysis for stable intracontinental regions (Seo *et al.*, 2009; Petersen *et al.*, 2014; So *et al.*, 2016; Wheeler, 2016; Kim and Lee, 2017). We implement the maximum magnitudes of M_w 6.8, 7.0, and 7.2 with weights of 0.25, 0.5, and 0.25, respectively, to cover a plausible range of maximum magnitudes (Woessner *et al.*, 2015) (Fig. 12).

We assign the weights for the GMPEs by considering the fitness with field observations as well as data sets and methods (Bommer *et al.*, 2010; Petersen *et al.*, 2014) (Figs. 11 and 12). Models GE1–GE5 are synthetic experiment-based GMPEs, and models GE6 and GE7 are field observation-based GMPEs. Model GE3 presents the best fitness with observed ground motions. Models GE1 and GE4 present relatively low fitness (Fig. 11). We assign larger weights in the order of GE3, GE5, GE2, GE1, and GE4 (Figs. 11 and 12). Model GE7 fits better than model GE6. Model GE7 was calibrated for large events compared to model GE6 (Table 2). We assign a larger weight to model GE7 than model GE6 (Figs. 11 and 12).

VALIDATION TEST

PSHA incorporates a series of numerical processes. We examine the process validity using a Monte Carlo simulation of ground-motion level exceedance rates (Musson, 2012; Hale *et al.*, 2018). We produce synthetic earthquake records for 100 million years that simulate a sufficiently long period to experience all possible

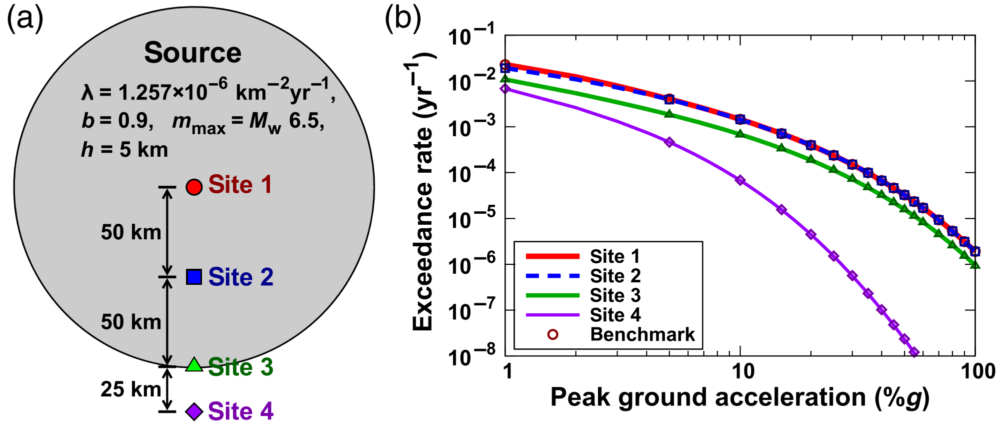

Figure 14. Benchmark test of PSHA: (a) fictitious source and site locations, and (b) comparison between benchmark results (open symbols) from Hale *et al.* (2018) and ground-motion level exceedance rates from PSHA (lines). Source model parameters including seismicity rate (λ), b-value, maximum magnitude (m_{max}), and source depth (h) are denoted. The PSHA results coincide with the benchmark results. The color version of this figure is available only in the electronic edition.

earthquakes. The study area is discretized by $0.1° \times 0.1°$ cells. The numbers of earthquakes in cells satisfy the seismicity rates (Fig. 13). We determine the temporal distribution of earthquakes using a Poisson distribution function.

We perform the Monte Carlo simulation for one model-parameter set in logic tree. The earthquake magnitudes are selected stochastically so as to satisfy the Gutenberg–Richter magnitude–frequency relationship (Fig. 13). We consider the maximum magnitude of M_w 7.0 and source depth of 10 km. We also consider the seismicity rates for the seismotectonic province model SP1 and instrumental b-values. We apply the GMPE model GE1. We calculate the PGAs at Seoul (37.6° N, 127° E) by the synthetic events (Fig. 13). We add random Gaussian errors with standard deviation (σ_Y) of 0.26 to the PGAs.

We determine the ground-motion level exceedance rates based on the synthetic ground-motion levels (Fig. 13). We compare the ground-motion level exceedance rates based on the synthetic earthquake data with those from PSHA. We find that the PSHA results match with the simulation results (Fig. 13). The synthetic test verifies the PSHA process.

We examine the validity of codes through benchmark tests for designed situations (Hale *et al.*, 2018). We consider a circular source area with a radius of 100 km and seismicity rate of 1.257×10^{-6} km^{-2} yr^{-1} (Fig. 14). The b-value, maximum magnitude, and source depth are set to be 0.9, M_w 6.5, and

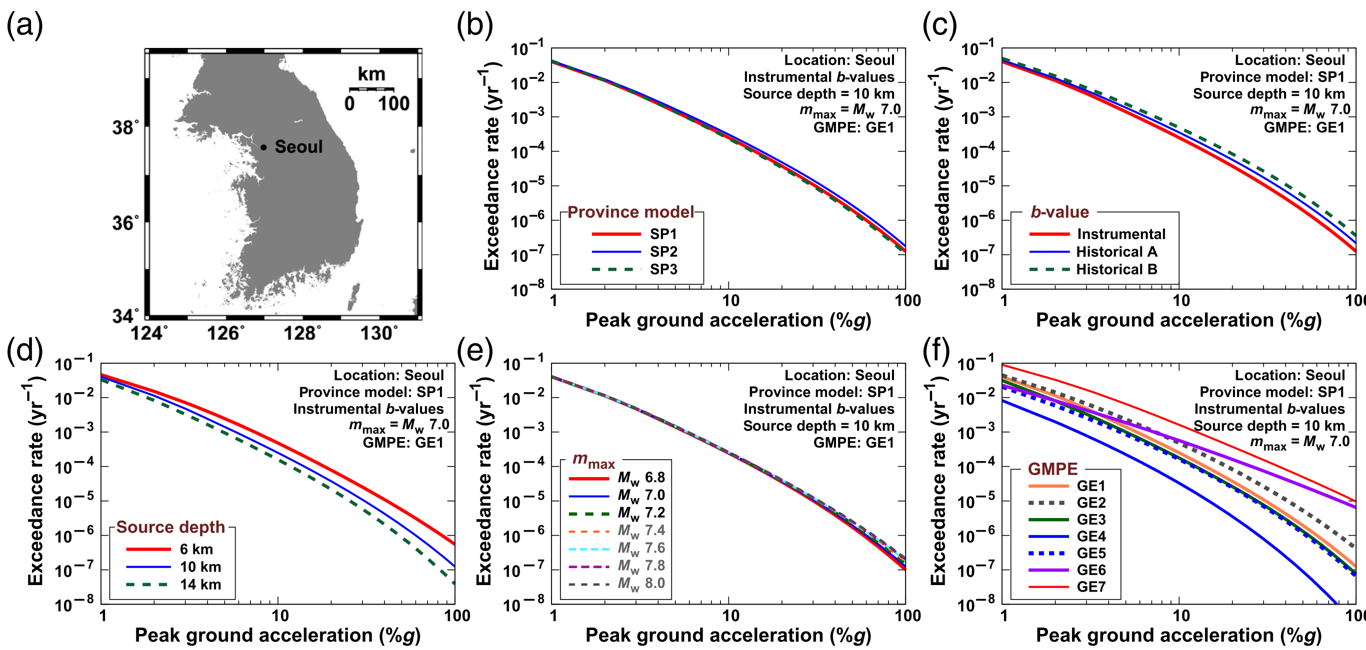

Figure 15. Sensitivity test of model parameters in PSHA: (a) map of test site (Seoul) and changes of ground-motion level exceedance rate curves by (b) seismotectonic province model, (c) b-value, (d) source depth, (e) maximum magnitude (m_{max}), and (f) GMPE. The input model parameters are denoted. The color version of this figure is available only in the electronic edition.

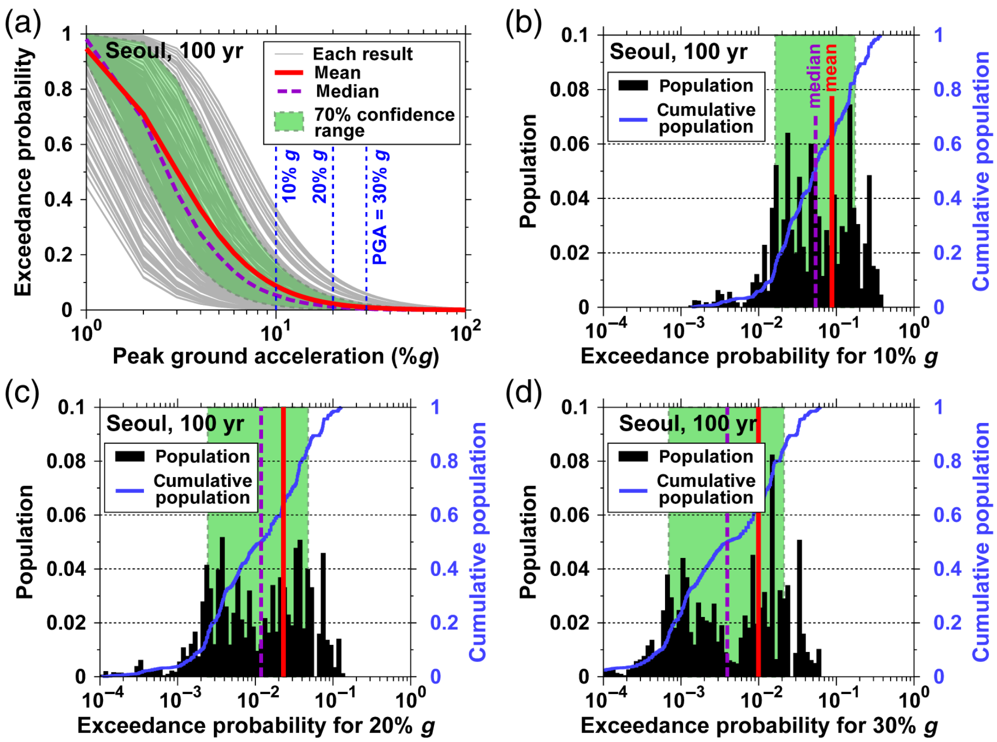

Figure 16. Ground-motion level exceedance probabilities for model-parameter sets from logic tree: (a) exceedance probability of peak ground accelerations (PGAs) at Seoul for the period of 100 yr, and population of ground-motion level exceedance probabilities for (b) 0.1*g*, (c) 0.2*g*, and (d) 0.3*g*. The weighted mean (solid line), median (dotted line), and 70% confidence range (shaded) in the exceedance probabilities are presented. The color version of this figure is available only in the electronic edition.

5 km, respectively. We implement a ground-motion attenuation equation for California (Sadigh *et al.*, 1997). We calculate the exceedance rates of ground-motion levels at distances of 0, 50, 100, and 125 km from the center of the source area.

We perform the PSHA for the given set of seismic source and ground-motion model. We compare the results with benchmark results (Hale *et al.*, 2018) (Fig. 14). The differences between the results are less than 2% in all distances, suggesting the validity of PSHA process and results.

SENSITIVITY TEST

We examine the sensitivity of PSHA results to input model parameters (Marzocchi *et al.*, 2015). We calculate the ground-motion level exceedance-rate curves for given sets of input model parameters (Fig. 15). We consider the ground motions at a site in Seoul.

We find that the ground-motion level exceedance rate curves are similar among different seismotectonic province models (Fig. 15b). This feature may be because the seismicity properties are represented comparably among different seismotectonic province models (Figs. 5 and 8). The ground-motion level exceedance rate curve for the seismotectonic province-based instrumental earthquake *b*-values is slightly lower than those for the historical earthquake *b*-values. This may be because the seismotectonic province-based instrumental earthquake *b*-values are slightly higher than the historical earthquake *b*-values in most areas (Fig. 15c).

Source depth significantly affects the ground-motion level exceedance rate (Fig. 15d). Fractional changes in shallow source depths may affect ground motions and exceedance rates.

The ground-motion level exceedance rates are determined comparable among the cases with maximum magnitudes M_w 6.8–8.0. This is because the occurrence frequencies of such large-magnitude events are so small for the considered recurrence periods. The observation may suggest that possible under- or overestimation of maximum magnitudes may negligibly affect the ground-motion level exceedance rate in PSHA for the Korean Peninsula. We choose three representative maximum magnitudes (M_w 6.8, 7.0, and 7.2) considering the observed seismicity in and around the Korean Peninsula (M_w 6.8, 7.0, and 7.2) (Fig. 15e).

The ground-motion level exceedance rate highly varies with the GMPE (Fig. 15f). Model GE7 yields the largest ground-motion level exceedance rates. On the other hand, model GE4 presents the lowest ground-motion level exceedance rates. The highest and lowest hazard curves differ by a factor of hundreds for the given input model parameter set.

We calculate the exceedance probability of PGAs for all possible combinations of input model parameters for the period of 100 yr (Fig. 16). The 70% confidence ranges of exceedance probabilities are 1.6%–17.5% for 0.1*g*, 0.2%–4.8% for 0.2*g*, and 0%–2.1% for 0.3*g*. The median values of exceedance probabilities are 5.4%, 1.2%, and 0.4%, close to the logarithmic mean values (8.8%, 2.3%, and 1.0%).

The ground-motion level exceedance probabilities vary by region (Fig. 17). Pyongyang and Ulsan present relatively large exceedance probabilities. On other hand, Gwangju shows low-exceedance probability. The mean exceedance probability curve for Pyongyang is larger than that for Gwangju by a factor of ~2.

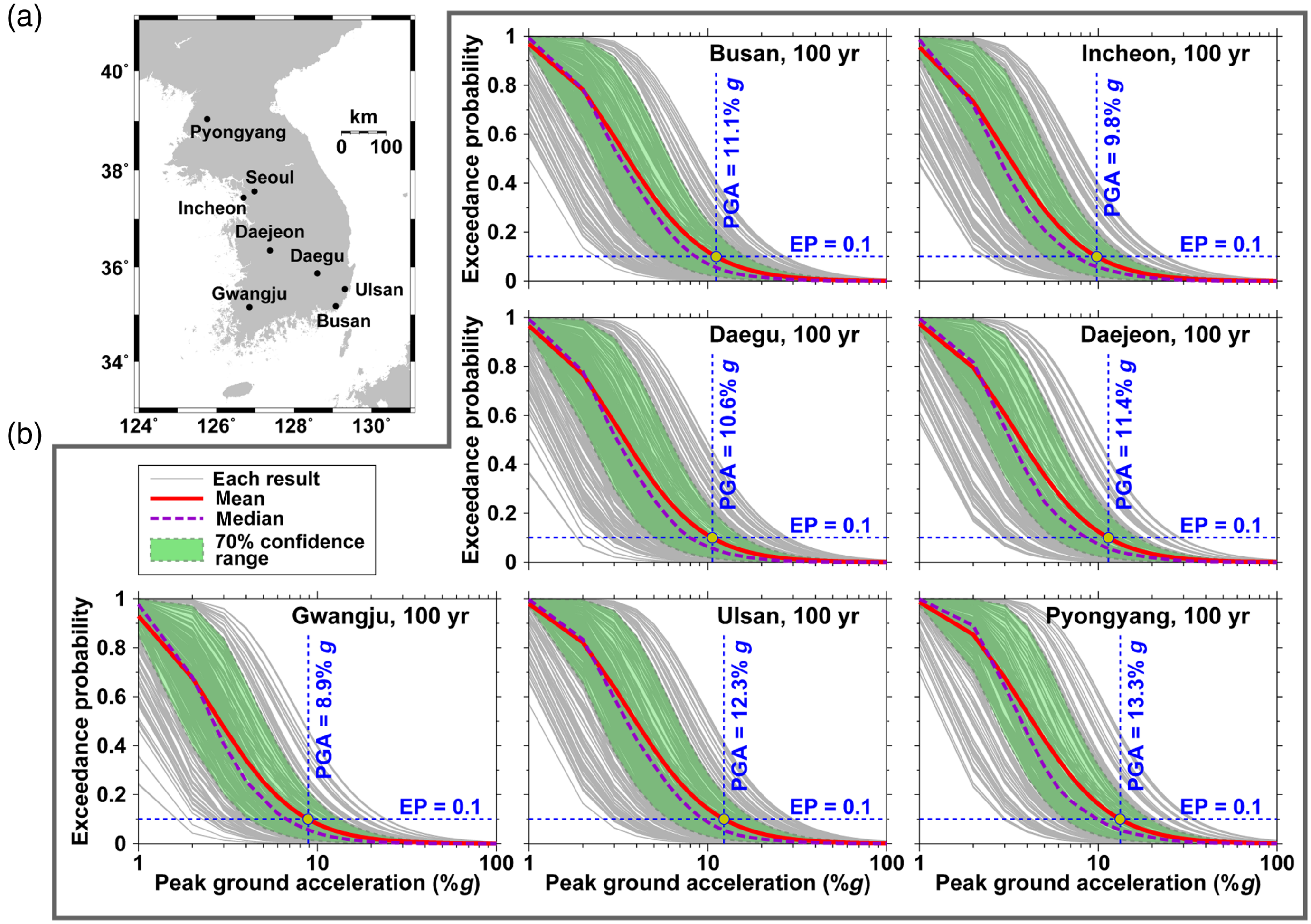

Figure 17. Seismic hazard analysis for major cities in the Korean Peninsula: (a) locations of major cities including Busan, Incheon, Daegu, Daejeon, Gwangju, Ulsan, and Pyongyang, and (b) ground-motion level exceedance probabilities in the major cities for the period of 100 yr. The weighted means (solid lines), medians (dotted lines), and 70% confidence ranges (shaded) in the exceedance probabilities are presented. The PGAs for exceedance probability of 10% are denoted. The color version of this figure is available only in the electronic edition.

SEISMIC HAZARD MAP

We calculate the PGAs with exceedance probability of 10% for periods of 25, 50, 100, 250, and 500 yr, based on the logic-tree scheme (Fig. 18). The spatial distribution of expected PGAs is generally similar to the seismicity distribution (Fig. 18). Strong ground motions are expected in the northwestern and southeastern Korean Peninsula. The PGAs with exceedance probability of 10% for the periods of 25, 50, 100, 250, and 500 yr in the northwestern and southeastern Korean Peninsula are ~0.06*g*, 0.09*g*, 0.13*g*, 0.21*g*, and 0.28*g*.

We observe relatively high-seismic hazard potentials in the south-central Korean Peninsula. The PGAs with exceedance probability of 10% for the periods of 25, 50, 100, 250, and 500 yr are 0.05*g*, 0.08*g*, 0.11*g*, 0.18*g*, and 0.25*g*, respectively. We find relatively low-seismic hazards in the northern, central, and southwestern Korean Peninsula (Fig. 18). The PGAs are smaller than 0.05*g*, 0.07*g*, 0.1*g*, 0.15*g*, and 0.22*g*.

We investigate the occurrence probabilities that the PGAs exceed 0.1*g*, 0.2*g*, and 0.3*g* in 50, 100, 250, and 500 yr (Fig. 19). The exceedance probabilities for 0.1g in 50, 100, and 250 yr are larger than 4%, 8%, and 16%, respectively, in most regions. The exceedance probabilities for 0.1*g* in 500 yr are larger than 28% in most regions. In particular, the occurrence probabilities reach 48%, 44%, and 40% in the northwestern, southeastern, and south-central Korean Peninsula. The exceedance probabilities for 0.2*g* in 50, 100, and 250 yr are lower than 10% in the most regions. The exceedance probabilities for 0.2*g* in 500 yr are larger than 8% in the most regions, reaching 20%, 18%, and 14% in the northwestern, southeastern, and south-central Korean Peninsula, respectively. The exceedance probabilities of PGAs for 0.3g are lower than 10% in the most regions at all periods.

SEISMIC HAZARD IMPLICATION

We find relatively high-seismic hazard potentials around major cities, including Busan, Daegu, Daejeon, Pyongyang, and Ulsan (Figs. 17–19). The spatial variation in exceedance

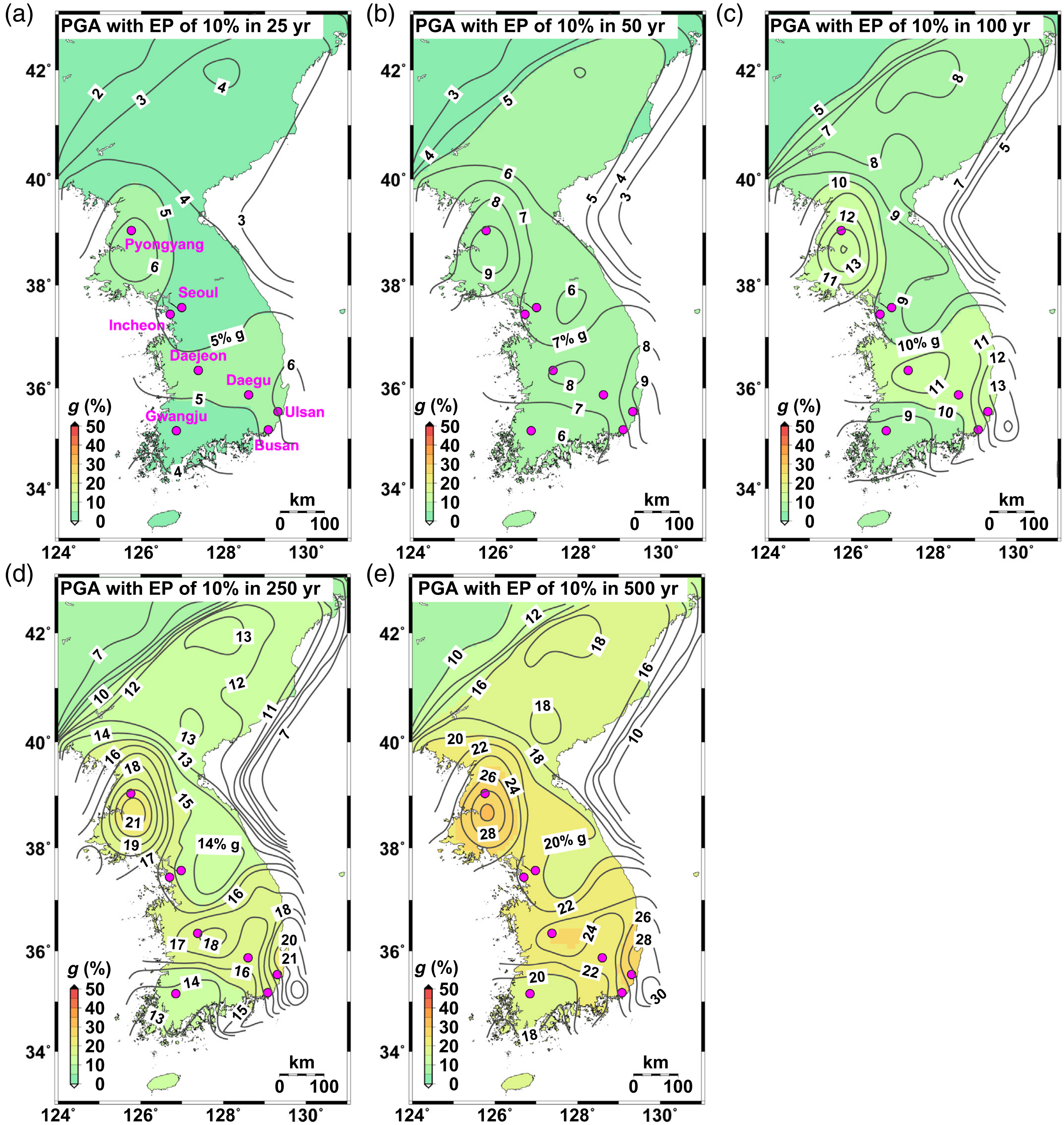

probabilities of peak ground motions is generally consistent with historical seismic-damage records (Houng and Hong, 2013) (Fig. 3). Historical records include high-seismic damages in the northwestern and southern Korean Peninsula (Lee and Yang, 2006; Houng and Hong, 2013). On the other hand, we observe relatively low-seismic hazard potentials in the west-central and southwestern Korean Peninsula where major historical seismic damages were reported (Park *et al.*, 2020).

Figure 18. Seismic hazard maps of the Korean Peninsula for PGAs with exceedance probability of 10% for periods of (a) 25, (b) 50, (c) 100, (d) 250, and (e) 500 yr. Major cities are marked (closed circles). Seismic hazard potentials are high in the northwestern, south-central, and southeastern Korean Peninsula. The color version of this figure is available only in the electronic edition.

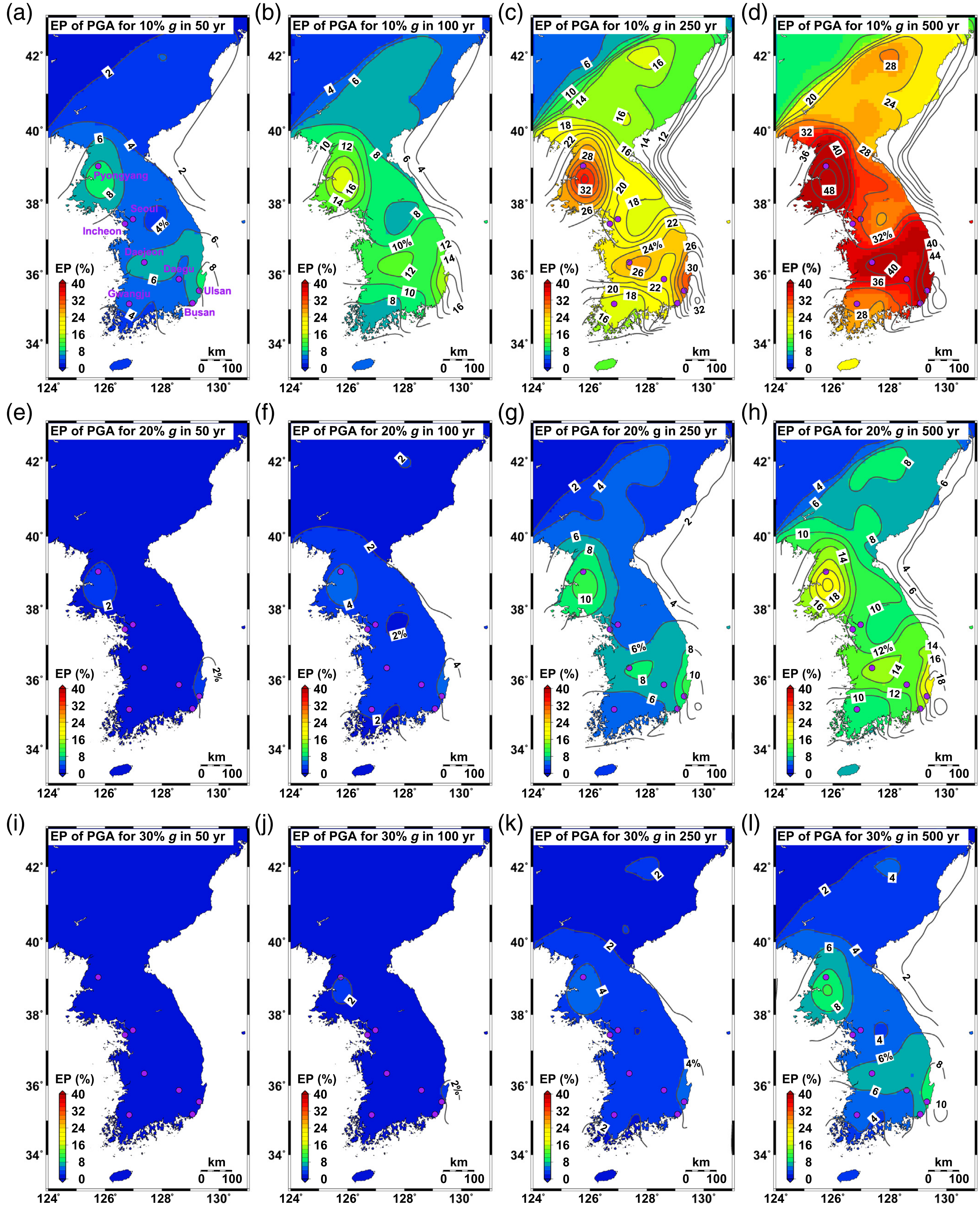

Figure 19. Ground-motion level exceedance probabilities for PGA of 0.1g for periods of (a) 50, (b) 100, (c) 250, and (d) 500 yr, those of 0.2g for periods of (e) 50, (f) 100, (g) 250, and (h) 500 yr, and those of 0.3g for periods of (i) 50, (j) 100, (k) 250, and (l) 500 yr. Major cities are marked (closed circles). The color version of this figure is available only in the electronic edition.

The relatively high-seismic hazard potentials around the northwestern and south-central Korean Peninsula are consistent with previous studies (Fig. 18) (Ministry of Construction and Transportation, 1997; Giardini *et al.*, 1999; Zhang *et al.*, 1999; National Emergency Management Agency, 2012; Kyung *et al.*, 2016). It was reported that the PGAs of the exceedance probability of 10% for periods of 50, 100, 250, and 500 yr are 0.07–0.10g, 0.11–0.14*g*, 0.17–0.19g, and 0.23–0.25*g* in the south-central Korean Peninsula, and 0.09–0.10g, 0.12–0.13*g*, 0.19–0.20*g*, and 0.25–0.28*g* in the northwestern Korean Peninsula (Ministry of Construction and Transportation, 1997; Giardini *et al.*, 1999; Zhang *et al.*, 1999; National Emergency Management Agency, 2012; Kyung *et al.*, 2016). We additionally find high-seismic hazard potentials in the southeastern Korean Peninsula.

The seismic hazard potentials around the Korean Peninsula generally agree with those in adjacent regions and other intraplate regions, including eastern Russia, northeastern China, eastern North America, central and northern Europe, Britain, and western and southeastern Australia (Giardini *et al.*, 1999; Ulomov and the GSHAP Region 7 Working Group, 1999; Zhang *et al.*, 1999; Petersen *et al.*, 2014; Woessner *et al.*, 2015; Allen *et al.*, 2019). The exceedance probabilities of peak ground motions in the Korean Peninsula are larger than those in low-seismicity regions such as central Russia, central and western Africa, and northeastern Australia (Giardini *et al.*, 1999; Ulomov and the GSHAP Region 7 Working Group, 1999; Allen *et al.*, 2019). On the other hand, the seismic hazard potentials in the Korean Peninsula are generally lower than those in active tectonic regions such as the western North America and Japanese islands (Fujiwara *et al.*, 2009; Petersen *et al.*, 2014).

DISCUSSION AND CONCLUSIONS

We performed a seismic hazard analysis for the Korean Peninsula. The source models were determined based on up-to-date earthquake catalogs. The GMPEs were examined with field observations before application to seismic hazard analysis. The PSHA results present relatively high seismic hazard potentials in the northwestern, south-central, and southeastern Korean Peninsula, and relatively low-seismic hazard potentials in the northern, central, and southwestern Korean Peninsula. It is noteworthy that major cities including Busan, Daegu, Daejeon, Ulsan, and Pyongyang are placed around regions with relatively high-seismic hazard potential.

Overall spatial variations in seismic hazard potentials agree with previous studies (Ministry of Construction and Transportation, 1997; Giardini *et al.*, 1999; National Emergency Management Agency, 2012; Kyung *et al.*, 2016). We additionally found high-seismic hazard potentials in the southeastern Korean Peninsula, which are associated with recent high seismicity (Hong, Park, Lee, and Kim, 2020). It is noteworthy that the 12 September 2016 M_w 5.4 earthquake and the 15 November 2017 M_w 5.5 earthquakes induced strong ground accelerations exceeding 0.45*g* and 0.20*g* in the region (Hong *et al.*, 2017, 2018). The recent moderate-size earthquakes since the 11 March 2011 Tohoku–Oki megathrust earthquake increased the seismic hazard potentials in the southeastern peninsula.

The seismic hazard analysis of this study presents the ground-motion amplitudes on bedrock. The ground-motion levels on the surface are highly dependent on the site conditions (e.g., Joyner and Boore, 1988; Wang and Hao, 2002; Pratt *et al.*, 2003). The subsurface structure may amplify the ground motions. It is desirable to take into account the site effects for practical application of the results. Also, it is noteworthy that the crustal structure may serve an additional role in seismic amplification. For instance, seismic waves are highly amplified in the crust of the southern Korean Peninsula (Hong and Lee, 2012; Park and Hong, 2017).

We performed the seismic hazard analysis mainly based on seismicity data. The geometry and properties of active faults were poorly specified in the Korean Peninsula, which is partly because most seismic activity occurs in subsurface hidden faults with no apparent surface ruptures (e.g., Hong *et al.*, 2017). Future studies may combine the fault sources to improve the seismic hazard assessment (e.g., Fujiwara *et al.*, 2009; Petersen *et al.*, 2014).

DATA AND RESOURCES

The instrumental earthquake catalogs are available from the Korea Meteorological Administration (KMA, http://necis.kma.go.kr/, last accessed May 2020), Japan Meteorological Agency (JMA, https://www.data.jma.go.jp/, last accessed May 2020), and International Seismological Centre (ISC, http://www.isc.ac.uk/iscbulletin/, last accessed May 2020). The moment magnitudes for instrumental earthquakes are partly collected from the Global Centroid Moment Tensor project (Global CMT, https://www.globalcmt.org/, last accessed May 2020). The seismic waveforms were collected from the KMA (http://necis.kma.go.kr/, last accessed May 2020) and Korea Institute of Geoscience and Mineral Resources (KIGAM, https://www.kigam.re.kr/, last accessed January 2018).

DECLARATION OF COMPETING INTERESTS

The authors declare that there are no competing interests recorded.

ACKNOWLEDGMENTS

The authors thank two anonymous reviewers and associate editor Mark Stirling for constructive review comments. This work was supported by the Korea Meteorological Administration Research and Development Program under Grant Number KMI2018-02910. In addition, this research was partly supported by the Basic Science Research Program of National Research Foundation of Korea (NRF-2017R1A6A1A07015374, NRF-2018R1D1A1A09083446).

REFERENCES

Allen, T. I., J. D. Griffin, M. Leonard, D. J. Clark, and H. Ghasemi (2019). The 2018 National seismic hazard assessment of

Australia: Quantifying hazard changes and model uncertainties, *Earthq. Spectra* doi: 10.1177/8755293019900777.

Atkinson, G. M., and D. M. Boore (2006). Earthquake ground-motion prediction equations for eastern North America, *Bull. Seismol. Soc. Am.* **96,** 2181–2205.

Baker, J. W. (2008). An introduction to probabilistic seismic hazard analysis (PSHA), Version 1.3, 72 pp.

Bender, B. (1983). Maximum likelihood estimation of b values for magnitude grouped data, *Bull. Seismol. Soc. Am.* **73,** 831–851.

Bender, B. K., and D. M. Perkins (1993). Treatment of parameter uncertainty and variability for a single seismic hazard map, *Earthq. Spectra* **9,** 165–195.

Bommer, J. J., J. Douglas, F. Scherbaum, F. Cotton, H. Bungum, and D. Fäh (2010). On the selection of ground-motion prediction equations for seismic hazard analysis, *Seismol. Res. Lett.* **81,** 783–793.

Bormann, P., R. Liu, R. X. Ren, R. Gutdeutsch, D. Kaiser, and S. Castellaro (2007). Chinese national network magnitudes, their relation to NEIC magnitudes and recommendations for new IASPEI magnitude standards, *Bull. Seismol. Soc. Am.* **97,** 114–127.

Cho, H.-M., H.-J. Kim, H.-T. Jou, J.-K. Hong, and C.-E. Baag (2004). Transition from rifted continental to oceanic crust at the southeastern Korean margin in the East Sea (Japan Sea), *Geophys. Res. Lett.* **31,** L07606, doi: 10.1029/2003GL019107.

Cho, J.-D., J.-H. Choi, M.-T. Lim, I.-H. Park, and I.-S. Ko (1997). A study on the regional gravity anomaly (Southern Part of Korean Peninsula), *KIGAM Res. Rept. KR-96 (c)-5*, Korea Institute of Geology and Mining and Materials, 27 pp. (in Korean).

Choi, H., T.-K. Hong, X. He, and C.-E. Baag (2012). Seismic evidence for reverse activation of a paleo-rifting system in the East Sea (Sea of Japan), *Tectonophysics* **572/573,** 123–133.

Choi, H., M. Noh, and K. Choi (2004). The relation between local magnitude and moment magnitude in the southern part of the Korean Peninsula, *J. Korean Geophys. Soc.* **7,** 183–192 (in Korean).

Choi, S.-J., U. Chwae, H.-K. Lee, Y. Song, and I.-M. Kang (2012). Review on the Chugaryeong Fault, *J. Korean Soc. Econ. Environ. Geol.* **45,** 441–446 (in Korean).

Chough, S. K., S.-T. Kwon, J.-H. Ree, and D. K. Choi (2000). Tectonic and sedimentary evolution of the Korean peninsula: A review and new view, *Earth Sci. Rev.* **52,** 175–235.

Chung, T. W., M. Z. Iqbal, Y. Lee, K. Yoshimoto, and J. Jeong (2018). Depth-dependent seismicity and crustal heterogeneity in South Korea, *Tectonophysics* **749,** 12–20.

Cornell, C. A. (1968). Engineering seismic risk analysis, *Bull. Seismol. Soc. Am.* **58,** 1583–1606.

Dziewonski, A. M., T.-A. Chou, and J. H. Woodhouse (1981). Determination of earthquake source parameters from waveform data for studies of global and regional seismicity, *J. Geophys. Res.* **86,** 2825–2852, doi: 10.1029/JB086iB04p02825.

Ekström, G., M. Nettles, and A. M. Dziewonski (2012). The global CMT project 2004-2010: Centroid-moment tensors for 13,017 earthquakes, *Phys. Earth Planet. In.* **200/201,** 1–9, doi: 10.1016/j.pepi.2012.04.002.

Emolo, A., N. Sharma, G. Festa, A. Zollo, V. Convertito, J.-H. Park, H.-C. Chi, and I.-S. Lim (2015). Ground-motion prediction equations for South Korea Peninsula, *Bull. Seismol. Soc. Am.* **105,** 2625–2640.

Frankel, A. (1995). Mapping seismic hazard in the central and eastern United States, *Seismol. Res. Lett.* **66,** 8–21.

Fujiwara, H., S. Kawai, S. Aoi, N. Morikawa, S. Senna, N. Kudo, M. Ooi, K. X. Hao, K. Wakamatsu, Y. Ishikawa, *et al.* (2009). Technical reports on national seismic hazard maps for Japan, *Technical Note of the National Research Institute for Earth Science and Disaster Prevention Number 336*, 528 pp.

Fujiwara, H., N. Morikawa, S. Kawai, S. Aoi, S. Senna, T. Maeda, H. Azuma, K. X. Hao, A. Iwaki, K. Wakamatsu, *et al.* (2015). Improved seismic hazard assessment after the 2011 Great East Japan Earthquake, *Technical Note of the National Research Institute for Earth Science and Disaster Prevention Number 399*, 253 pp. (in Japanese).

Gardner, J. K., and L. Knopoff (1974). Is the sequence of earthquakes in Southern California, with aftershocks removed, Poissonian? *Bull. Seismol. Soc. Am.* **64,** 1363–1367.

Gerstenberger, M., S. Wiemer, and D. Giardini (2001). A systematic test of the hypothesis that the b value varies with depth in California, *Geophys. Res. Lett.* **28,** 57–60.

Giardini, D., G. Grünthal, K. M. Shedlock, and P. Zhang (1999). The GSHAP global seismic hazard map, *Ann. Geophys.* **42,** 1225–1230.

Gutenberg, B., and C. F. Richter (1956). Earthquake magnitude, intensity, energy, and acceleration (second paper), *Bull. Seismol. Soc. Am.* **46,** 105–145.

Hale, C., N. Abrahamson, and Y. Bozorgnia (2018). Probabilistic seismic hazard analysis code verification, *PEER Rept. No. 2018/03*, Pacific Earthquake Engineering Research Center, 120 pp.

Han, Q., L. Wang, J. Xu, A. Carpinteri, and G. Lacidogna (2015). A robust method to estimate the b-value of the magnitude-frequency distribution of earthquakes, *Chaos, Solitons & Fractals* **81,** 103–110.

Hong, T.-K. (2010). *Lg* attenuation in a region with both continental and oceanic environments, *Bull. Seismol. Soc. Am.* **100,** 851–858.

Hong, T.-K. (2012). *Lg* body-wave magnitude scaling for the continental margin around the Korean Peninsula, *Pure Appl. Geophys.* **169,** 641–658.

Hong, T.-K., and H. Choi (2012). Seismological constraints on the collision belt between the North and South China blocks in the Yellow Sea, *Tectonophysics* **570/571,** 102–113.

Hong, T.-K., and T.-S. Kang (2009). *Pn* travel-time tomography of the paleo-continental-collision and rifting zone around Korea and Japan, *Bull. Seismol. Soc. Am.* **99,** 416–421.

Hong, T.-K., and K. Lee (2012). $m_b(Pn)$ scale for the Korean Peninsula and site-dependent *Pn* amplification, *Pure Appl. Geophys.* **169,** 1963–1975.

Hong, T.-K., C.-E. Baag, H. Choi, and D.-H. Sheen (2008). Regional seismic observations of the 9 October 2006 underground nuclear explosion in North Korea and the influence of crustal structure on regional phases, *J. Geophys. Res.* **113,** B03305, doi: 10.1029/2007JB004950.

Hong, T. K., E. Choi, S. Park, and J. S. Shin (2016). Prediction of ground motion and dynamic stress change in Baekdusan (Changbaishan) volcano caused by a North Korean nuclear explosion, *Sci. Rep.* **6,** 1–8.

Hong, T.-K., J. Lee, and S. E. Houng (2015). Long-term evolution of intraplate seismicity in stress shadows after a megathrust, *Phys. Earth Planet. In.* **245,** 59–70.

Hong, T.-K., J. Lee, W. Kim, I.-K. Hahm, N. C. Woo, and S. Park (2017). The 12 September 2016 M_L 5.8 mid-crustal earthquake in the Korean Peninsula and its seismic implications, *Geophys. Res. Lett.* **44,** 3131–3138, doi: 10.1002/2017GL072899.

Hong, T.-K., J. Lee, S. Park, and W. Kim (2018). Time-advanced occurrence of moderate-size earthquakes in a stable intraplate region after a megathrust earthquake and their seismic properties, *Sci. Rep.* **8,** 1–8, doi: 10.1038/s41598-018-31600-5.

Hong, T.-K., S. Park, and S. E. Houng (2016). Seismotectonic properties and zonation of the far-eastern Eurasian plate around the Korean Peninsula, *Pure Appl. Geophys.* **173,** 1175–1195.

Hong, T.-K., S. Park, J. Lee, D. Chung, and W. Kim (2020). One-off deep crustal earthquake swarm in a stable intracontinental region of the southwestern Korean Peninsula, *Phys. Earth Planet. In.* **308,** 106582, doi: 10.1016/j.pepi.2020.106582.

Hong, T.-K., S. Park, J. Lee, and W. Kim (2020). Spatiotemporal seismicity evolution and seismic hazard potentials in the western East Sea (Sea of Japan), *Pure Appl. Geophys.* **177,** no. 8, 3761–3774.

Hough, S. E. (2013). Spatial variability of "Did You Feel It?" intensity data: Insights into sampling biases in historical earthquake intensity distributions, *Bull. Seismol. Soc. Am.* **103,** 2767–2781.

Houng, S. E., and T.-K. Hong (2013). Probabilistic analysis of the Korean historical earthquake records, *Bull. Seismol. Soc. Am.* **103,** 2782–2796.

Jo, E., and T.-K. Hong (2013). V_P/V_Sratios in the upper crust of the southern Korean Peninsula and their correlations with seismic and geophysical properties, *J. Asian Earth Sci.* **66,** 204–214.

Jo, N.-D., and C.-E. Baag (2003). Estimation of spectrum decay parameter x and stochastic prediction of strong ground motions in Southeastern Korea, *J. Earthq. Eng. Soc. Korea* **7,** 59–70 (in Korean).

Jolivet, L., K. Tamaki, and M. Fournier (1994). Japan Sea, opening history and mechanism: A synthesis, *J. Geophys. Res.* **99,** 22,237–22,259.

Joyner, W. B., and D. M. Boore (1988). Measurement, characterization, and prediction of strong ground motion, *Proc. of Earthquake Engineering and Soil Dynamics II*, GT div/ASCE, Park City, Utah, 27–30 June 1988, 43–102.

Jun, M.-S., and J.-S. Jeon (2001). Early instrumental earthquake data (1905-1942) in Korea, *Econ. Environ. Geol.* **34,** 573–581 (in Korean).

Jun, M.-S., and J.-S. Jeon (2010). Focal mechanism in and around the Korean peninsula, *Geophys. Geophys. Explor.* **13,** 198–202 (in Korean).

Katsumata, A. (1996). Comparison of magnitudes estimated by the Japan Meteorological Agency with moment magnitudes for intermediate and deep earthquakes, *Bull. Seismol. Soc. Am.* **86,** 832–842.

Khan, P. K., M. Ghosh, P. P. Chakraborty, and D. Mukherjee (2011). Seismic *b*-value and the assessment of ambient stress in Northeast India, *Pure Appl. Geophys.* **168,** 1693–1706.

Kijko, A., and M. Singh (2011). Statistical tools for maximum possible earthquake magnitude estimation, *Acta Geophys.* **59,** 674–700.

Kim, S. K., and J. M. Lee (2017). Probabilistic seismic hazard analysis using a synthetic earthquake catalog: Comparison of the Gyeongju City Hall site with the Seoul City Hall site in Korea, *Geosci. J.* **21,** 523–533.

Korea Hydro and Nuclear Power (2015). Investigation and research on the largest Earthquake around Nuclear Power Plant Sites (I), Korea Hydro and Nuclear Power, 402 pp. (in Korean).

Korea Meteorological Administration (2012). Historical earthquake records in Korea (2:1904), Korea Meteorological Administration, Seoul, Korea, 279 pp. (in Korean).

Kyung, J. B. (2010). Paleoseismological study and evaluation of maximum earthquake magnitude along the Yangsan and Ulsan Fault Zones in the Southeastern Part of Korea, *Geophys. Geophys. Explor.* **13,** 187–197 (in Korean).

Kyung, J. B., and K. Lee (2006). Active fault study of the Yangsan fault system and Ulsan fault system, southeastern part of the Korean Peninsula, *J. Korean Geophys. Soc.* **9,** 219–230.

Kyung, J.-B., M.-J. Kim, S.-J. Lee, and J.-K. Kim (2016). An analysis of probabilistic seismic hazard in the Korean Peninsula-Probabilistic peak ground acceleration (PGA), *J. Korean Earth Sci. Soc.* **37,** 52–61 (in Korean).

Lee, H.-K., and P. S. Henry (2001). ESR dating of the subsidiary faults in the Yangsan fault system, Korea, *Quaternary Sci. Rev.* **20,** 999–1003.

Lee, J., and T.-K. Hong (2014). Dynamic lithospheric response to megathrust and precursory seismicity features of megathrust, *Phys. Earth Planet. In.* **234,** 35–45.

Lee, J., T.-K. Hong, and C. Chang (2017). Crustal stress field perturbations in the continental margin around the Korean Peninsula and Japanese islands, *Tectonophysics* **718,** 140–149.

Lee, K., and W.-S. Yang (2006). Historical seismicity of Korea, *Bull. Seismol. Soc. Am.* **96,** 846–855.

Liu, J., Z. Wang, F. Xie, and Y. Lv (2013). Seismic hazard assessment for greater North China from historical intensity observations, *Eng. Geol.* **164,** 117–130.

Marsan, D., and O. Lengliné (2008). Extending earthquakes' reach through cascading, *Science* **319,** 1076–1079.

Marzocchi, W., and L. Sandri (2009). A review and new insights on the estimation of the *b*-value and its uncertainty, *Ann. Geophys.* **46,** 1271–1282.

Marzocchi, W., M. Taroni, and J. Selva (2015). Accounting for epistemic uncertainty in PSHA: Logic tree and ensemble modeling, *Bull. Seismol. Soc. Am.* **105,** 2151–2159.

Ministry of Construction and Transportation (1997). Investigation of seismic design standards (II): Seismic design standards and economic efficiency, *Rep. GOVP1199803210*, Ministry of Construction and Transportation, 493 pp. (in Korean).

Ministry of the Interior and Safety (2019). Development of standardized manual for National seismic hazard map, *Rep. 2017-MPSS31-007*, Ministry of the Interior and Safety, 632 pp. (in Korean).

Miyazawa, M., and J. Mori (2009). Test of seismic hazard map from 500 years of recorded intensity data in Japan, *Bull. Seismol. Soc. Am.* **99,** 3140–3149.

Moradpour, J., S. Hainzl, and J. Davidsen (2014). Nontrivial decay of aftershock density with distance in Southern California, *J. Geophys. Res.* **119,** 5518–5535.

Musson, R. M. W. (2012). PSHA validated by quasi observational means, *Seismol. Res. Lett.* **83,** 130–134.

National Emergency Management Agency (2012). Active fault map and seismic hazard map, *Rep. NEMA-NATURE-2009-24*, National Emergency Management Agency, 939 pp. (in Korean).

National Emergency Management Agency (2013). National Seismic Hazard Map Announcement, National Emergency Management Agency, National Emergency Management Agency Announcement 2013-179, 10 pp. (in Korean).

Oth, A., D. Bindi, S. Parolai, and D. Di Giacomo (2010). Earthquake scaling characteristics and the scale-(in)dependence of seismic energy-to-moment ratio: Insights from KiK-net data in Japan, *Geophys. Res. Lett.* **37,** doi: 10.1029/2010GL044572.

Park, D.-H., J. M. Lee, C.-E. Baag, and J. K. Kim (2001). Stochastic prediction of strong ground motions and attenuation equations in the southeastern Korean Peninsula, *J. Geol. Soc. Korea* **37,** 21–30 (in Korean).

Park, S., and T.-K. Hong (2017). Regional seismic intensity anomalies in the Korean Peninsula and its implications for seismic-hazard potentials, *Pure Appl. Geophys.* **174,** 2561–2579.

Park, S., I. Baek, and T.-K. Hong (2020). Six major historical earthquakes in the Seoul metropolitan area during the Joseon dynasty (1392-1910), *Bull. Seismol. Soc. Am.* **110,** 3037–3049, doi: 10.1785/0120200004.

Petersen, M. D., M. P. Moschetti, P. M. Powers, C. S. Mueller, K. M. Haller, A. D. Frankel, Y. Zeng, S. Rezaeian, S. C. Harmsen, O. S. Boyd, *et al.* (2014). Documentation for the 2014 update of the United States national seismic hazard maps, *U.S. Geol. Surv. Open-File Rept. 2014-1091*, 243 pp., doi: 10.3133/ofr20141091.

Pezeshk, S., A. Zandieh, and B. Tavakoli (2011). Hybrid empirical ground-motion prediction equations for eastern North America using NGA models and updated seismological parameters, *Bull. Seismol. Soc. Am.* **101,** 1859–1870.

Pratt, T. L., T. M. Brocher, C. S. Weaver, K. C. Creager, C. M. Snelson, R. S. Crosson, K. C. Muller, and A. M. Treéhu (2003). Amplification of seismic waves by the Seattle basin, Washington State, *Bull. Seismol. Soc. Am.* **93,** 533–545.

Rachman, A. N., and T. W. Chung (2016). Depth-dependent crustal scattering attenuation revealed using single or few events in South Korea, *Bull. Seismol. Soc. Am.* **106,** 1499–1508.

Reasenberg, P. (1985). Second-order moment of central California seismicity, 1969-1982, *J. Geophys. Res.* **90,** 5479–5495, doi: 10.1029/JB090IB07p05479.

Rhee, H.-M., J.-M. Seo, D.-H. Sheen, and I.-K. Choi (2012). Probabilistic seismic hazard analysis on metropolitan cities and counties in Korea, *J. Geol. Soc. Korea* **48,** 259–273 (in Korean).

Roberts, N. S., A. F. Bell, and I. G. Main (2015). Are volcanic seismic *b*-values high, and if so when? *J. Volcanol. Geoth. Res.* **308,** 127–141.

Rong, Y., X. Xu, J. Cheng, G. Chen, H. Magistrale, and Z.-K. Shen (2020). A probabilistic seismic hazard model for Mainland China, *Earthq. Spectra* **36,** 181–209, doi: 10.1177/8755293020910754.

Sadigh, K., C.-Y. Chang, J. A. Egan, F. Makdisi, and R. R. Youngs (1997). Attenuation relationships for shallow crustal earthquakes based on California strong motion data, *Seismol. Res. Lett.* **68,** 180–189.

Scordilis, E. M. (2006). Empirical global relations converting M_S and mb to moment magnitude, *J. Seismol.* **10,** 225–236.

Secanell, R., X. Goula, T. Susagna, J. Fleta, and A. Roca (2004). Seismic hazard zonation of Catalonia, Spain, integrating random uncertainties, *J. Seismol.* **8,** 25–40.

Seo, J.-M., M. Noh, C.-J. Chang, and K.-H. Yun (2009). Status of the PSHA in Korea for nuclear power plant sites, *Nucl. Eng. Tech.* **41,** 1255–1262.

Sheen, D.-H., T.-S. Kang, and J. Rhie (2018). A local magnitude scale for South Korea, *Bull. Seismol. Soc. Am.* **108,** 2748–2755.

So, M. M. L., T. Mote, and J. W. Pappin (2016). Seismic hazard assessment of South Korea, *Jpn. Geotech. Soc. Spec. Publ.* **2,** 755–760.

Stirling, M., G. McVerry, M. Gerstenberger, N. Litchfield, R. Van Dissen, K. Berryman, P. Barnes, L. Wallace, P. Villamor, R. Langridge, *et al.* (2012). National seismic hazard model for New Zealand: 2010 update, *Bull. Seismol. Soc. Am.* **102,** 1514–1542.

Ulomov, V. I., and , and the GSHAP Region 7 Working Group (1999). Seismic hazard of Northern Eurasia, *Ann. Geofisc.* **42,** 1023–1038.

Utsu, T., Y. Ogata, and R. S. Matsu'ura (1995). The centenary of the Omori formula for a decay law of aftershock activity, *J. Phys. Earth* **43,** 1–33.

Wang, S., and H. Hao (2002). Effects of random variations of soil properties on site amplification of seismic ground motions, *Soil Dynam. Earthq. Eng.* **22,** 551–564.

Wang, Y.-J., C.-H. Chan, Y.-T. Lee, K.-F. Ma, J. B. H. Shyu, R.-J. Rau, and C.-T. Cheng (2016). Probabilistic seismic hazard assessment for Taiwan, *Terr. Atmos. Ocean. Sci.* **27,** 325–340.

Weichert, D. H. (1980). Estimation of the earthquake recurrence parameters for unequal observation periods for different magnitudes, *Bull. Seismol. Soc. Am.* **70,** 1337–1346.

Wheeler, R. L. (2016). Maximum magnitude (M_{max}) in the Central and Eastern United States for the 2014 US Geological Survey hazard model, *Bull. Seismol. Soc. Am.* **106,** 2154–2167.

Wiemer, S., and M. Wyss (2000). Minimum magnitude of completeness in earthquake catalogs: Examples from Alaska, the western United States, and Japan, *Bull. Seismol. Soc. Am.* **90,** 859–869.

Woessner, J., D. Laurentiu, D. Giardini, H. Crowley, F. Cotton, G. Grünthal, G. Valensise, R. Arvidsson, R. Basili, M. B. Demircioglu, *et al.* (2015). The 2013 European seismic hazard model: Key components and results, *Bull. Earthq. Eng.* **13,** 3553–3596.

Yun, K.-H., D.-H. Park, C.-J. Chang, and T.-M. Sim (2008). Estimation of aleatory uncertainty of the ground-motion attenuation relation based on the observed data, *Proc. of EESK Conf. Spring*, Vol. 12, 116–123 (in Korean).

Zhang, P., Z. Yang, H. K. Gupta, S. C. Bhatia, and K. M. Shedlock (1999). Global seismic hazard assessment program (GSHAP) in Continental Asia, *Ann. Geophys.* **42,** 1167–1190.

Zhao, J. X., F. Jiang, P. Shi, H. Xing, H. Huang, R. Hou, Y. Zhang, P. Yu, X. Lan, D. A. Rhoades, *et al.* (2016). Ground-motion prediction equations for subduction slab earthquakes in Japan using site class and simple geometric attenuation functions, *Bull. Seismol. Soc. Am.* **106,** 1535–1551.

Manuscript received 10 August 2020
Published online 25 May 2021